

1 **This is a non-peer reviewed pre-print submitted to EarthArXiv. Subsequent versions of**  
2 **this manuscript may have slightly different content. The manuscript has been submitted**  
3 **to Water Resources Research for peer-review.**

4  
5  
6  
7  
8  
9  
10  
11 **Rapid Fault Leakage Modelling for CO<sub>2</sub>**  
12 **Storage in Saline Aquifers**

13 Hariharan Ramachandran <sup>1\*</sup>, Iain de Jonge-Anderson <sup>1</sup>, Ikhwanul Hafizi Musa <sup>2</sup>, Uisdean  
14 Nicholson <sup>1</sup>, Chee Phuat Tan <sup>3,4</sup>, Sebastian Geiger <sup>5</sup>, Florian Doster <sup>1</sup>

15 <sup>1</sup> Institute of GeoEnergy Engineering, Heriot-Watt University, Edinburgh, UK

16 <sup>2</sup> PETRONAS Research Sdn Bhd, Bangi, Malaysia

17 <sup>3</sup> PETRONAS Carigali Sdn Bhd, Kuala Lumpur, Malaysia

18 <sup>4</sup> EJ Geomechanics Consulting, Kuala Lumpur, Malaysia

19 <sup>5</sup> Department of Geoscience and Engineering, Delft University of Technology, Delft,  
20 Netherlands

21 \* Correspondence: Hariharan Ramachandran, email: [h.ramachandran@hw.ac.uk](mailto:h.ramachandran@hw.ac.uk),

22 X: @hariharram

23 ORCID: 0000-0001-5979-0930 (HR)

24

25

# 1 **Rapid Fault Leakage Modelling for CO<sub>2</sub> Storage in Saline Aquifers**

2 **Hariharan Ramachandran**<sup>1\*</sup>, **Iain de Jonge-Anderson**<sup>1</sup>, **Ikhwanul Hafizi Musa**<sup>2</sup>, **Uisdean**  
3 **Nicholson**<sup>1</sup>, **Chee Phuat Tan**<sup>3,4</sup>, **Sebastian Geiger**<sup>5</sup>, and **Florian Doster**<sup>1</sup>

4 <sup>1</sup> Institute of GeoEnergy Engineering, Heriot-Watt University, Edinburgh, UK

5 <sup>2</sup> PETRONAS Research Sdn Bhd, Bangi, Malaysia

6 <sup>3</sup> PETRONAS Carigali Sdn Bhd, Kuala Lumpur, Malaysia

7 <sup>4</sup> EJ Geomechanics Consulting, Kuala Lumpur, Malaysia

8 <sup>5</sup> Department of Geoscience and Engineering, Delft University of Technology, Delft,  
9 Netherlands

10 \* Correspondence: Hariharan Ramachandran, [h.ramachandran@hw.ac.uk](mailto:h.ramachandran@hw.ac.uk)

11 ORCID: 0000-0001-5979-0930 (HR)

## 12 **Abstract**

13 Simulating the fluid flow along fault zones at different scales is essential for predicting the CO<sub>2</sub>  
14 leakage and containment during injection and storage. However, this can be challenging,  
15 especially in the early stages of a storage project when knowledge of the reservoir and caprock  
16 is limited and the cost of obtaining the relevant data is high. This study develops a tool for fast  
17 screening of fault leakage at the site screening stage. The tool uses a vertically integrated  
18 reservoir model coupled with a newly developed upscaled fault leakage function based on  
19 source/sink relations. The fault is conceptualized as an increased vertical permeability through  
20 the caprock due to the presence of a fracture network in the damage zone and a reduced  
21 horizontal permeability in the reservoir due to fault throw and presence of a low-permeability  
22 fault core. The proposed tool is validated against numerical simulations demonstrating strong  
23 agreement in predicting leakage rates under varying reservoir conditions. The model's  
24 capabilities are further tested through simulation cases, including a field-scale application in  
25 the Malay Basin. These cases revealed key insights into the roles of fault permeability and fault

1 capillary entry pressure in controlling leakage and highlighted the importance of accurately  
2 characterizing these properties to mitigate risks. The computationally efficient model presented  
3 in this study is a valuable tool for quantifying uncertainties in key fault parameters, and other  
4 constitutive relations that affect the behaviour of the storage reservoir and potential fault  
5 leakage.

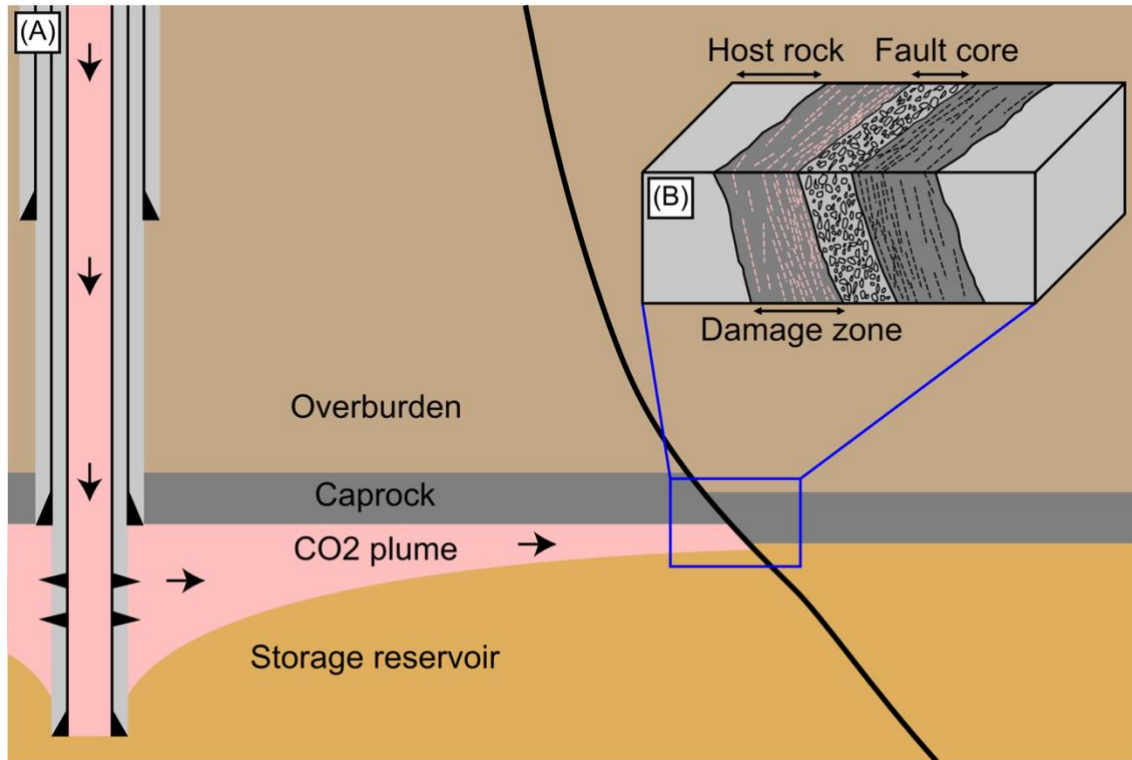
6 **Keywords:** CO<sub>2</sub> Leakage; Faults; CCS; Vertical Equilibrium Modelling; MRST.

## 7 1 Introduction

8 Storing CO<sub>2</sub> in geological formations is a crucial method for mitigating climate change  
9 and will be an essential component of a Net Zero Carbon Emission energy landscape in the  
10 coming decades (Hepple & Benson, 2004; Krevor et al., 2023). Among the most attractive  
11 storage options are saline aquifers, which are widely distributed and possess substantial total  
12 storage capacities exceeding gigatons of CO<sub>2</sub> globally (Kumar et al., 2004; Herzog, 2011; Celia  
13 et al., 2015). However, successful implementation hinges on the long-term secure containment  
14 of CO<sub>2</sub> within these aquifers. Leakage undermines mitigation efforts, poses  
15 environmental/health risks, and can erode public trust in Carbon Capture and Storage (CCS)  
16 (Bielicki et al., 2014; Ashworth et al., 2015; Jones et al., 2015). Regulatory bodies emphasize  
17 the importance of comprehensive geological characterization and storage site assessment to  
18 identify significant leakage risk (Dixon et al., 2015; Anderson, 2017; Climate Change  
19 Committee, 2021; Romanak & Dixon, 2022). In this context, faults play a crucial role as they  
20 can either increase or reduce storage potential, depending on host and fault rock properties. In  
21 some cases, by juxtaposing impermeable rock layers, they can function as structural traps,  
22 confining the injected CO<sub>2</sub> (Knipe et al., 1998; Pei et al., 2015). Conversely, faults also possess  
23 the potential to act as leakage pathways that connect the storage reservoir through the overlying  
24 caprock to shallower geological layers (Bachu, 2008; Rutqvist, 2012; Snippe et al., 2021). As  
25 the scale of CCS deployment increases, we will encounter numerous storage formations

1 containing faults, some of which may be sub-seismic, with uncertain properties. To expedite  
2 the storage site screening, rapid assessment tools are needed to screen for fault-related leakage  
3 risks during the early stages of project development.

4



5 Figure 1 – An illustrative representation of CO<sub>2</sub> storage in a faulted reservoir-caprock system.  
6 CO<sub>2</sub> is injected into permeable rock layers spanning hundreds of meters in thickness, with a  
7 low-permeability regional seal acting as the primary caprock. The presence of faults can either  
8 result in enhanced entrapment or vertical leakage, depending on fault properties (a). Schematic  
9 illustration of fault zone properties, including the fault core and adjacent damage zone (b).  
10 Figure adapted from Gasda et al. (2022).

11

12 Faults are complex zones of deformation characterized by a central zone of intensely  
13 sheared rock, referred to as the fault core, surrounded by a fractured damage zone with a  
14 progressively decreasing fracture density with increasing distance from the fault core (Figure  
15 1) (Sibson, 1977; Gillespie et al., 1993; Walsh et al., 1998; Childs et al., 2009; Faulkner et al.,  
16 2010; Ketterman et al 2020; Phillips et al., 2020). The fault core typically exhibits relatively  
17 low permeability because of cataclasis or clay smear (Bense & Person 2006; Tueckmantel et  
18 al., 2012; Ballas et al., 2015; Dewhurst et al., 2018), while the associated damage zones,

1 dominated by fractures, can exhibit permeabilities several orders of magnitude greater, which  
2 can increase their leakage potential (Caine et al., 1996; Childs et al., 2009; Seebeck et al., 2014).  
3 The critical fault properties controlling leakage through faulted zones include fault geometry,  
4 architecture, stress regime, and fracture density, among several others (Smith, 1980; Gibson,  
5 1998; Yielding et al., 2010; Rutqvist et al., 2012; Rizzo et al., 2024). Additionally, fault  
6 reactivation due to injection-induced changes in pore pressure and stress conditions can  
7 potentially generate new leakage pathways/fractures or alter existing ones (Tewari et al., 2023).  
8 Seismic imaging resolution limits the characterization of fine-scale features within the damage  
9 zone introducing uncertainties, as their presence, properties, and ability to form interconnected  
10 networks at larger scales remain poorly understood (Rizzo et al., 2024). This limited  
11 knowledge, particularly during the early stages of a CCS project when reservoir data is scarce  
12 and data acquisition expensive, can significantly hinder informed decision-making (Oladyshkin  
13 et al., 2011; Pawar et al., 2015; Pawar et al., 2016). Additionally, operators typically assess  
14 multiple potential storage sites in their portfolio, necessitating efficient screening methods to  
15 identify the most suitable storage candidates. This study focuses on pre-existing permeable fault  
16 zones and does not model fault reactivation or geomechanical-dynamic coupling. We consider  
17 these faults zones as a potential leakage pathway whose flow behaviour must be characterized.  
18 Stress-induced permeability changes, fault slip, and pressure-stress coupling are critical  
19 processes for comprehensive CCS risk assessment (Rinaldi, Rutqvist and Cappa, 2014; Jha and  
20 Juanes, 2014; Chang and Segall, 2016; Zhao and Jha, 2019; Meguerdijian and Jha, 2021; Chen  
21 et al., 2024) but require detailed site-specific geomechanical data rarely available during early-  
22 stage screening. These processes are best addressed through coupled geomechanical-dynamic  
23 models during later stages of site evaluation. However, by evaluating leakage across a wide  
24 uncertainty range of fault permeabilities - including values that may result from mechanical

1 processes - allows our screening approach to bound potential risks without explicitly modelling  
2 the underlying mechanisms.

3         Reservoir simulation plays a vital role in quantifying potential fault leakage rates for  
4 large-scale CO<sub>2</sub> storage modelling. In the context of this study, fault leakage refers to the  
5 upward migration of CO<sub>2</sub> along fault zones, driven by pressure gradients and buoyancy forces.  
6 This process occurs when faults act as vertical conduits, connecting storage reservoirs to  
7 overlying formations or the surface, potentially compromising the integrity of CO<sub>2</sub>  
8 containment. The implementation of faults in full reservoir simulations is typically limited to  
9 transmissibility multipliers, which adjust flow properties between adjacent grid blocks to reflect  
10 across fault permeability (Manzocchi et al., 1999). These multipliers cannot capture the  
11 interplay between fault permeability and vertical pressure gradients, and the overlying  
12 formations need to be explicitly gridded increasing the computation requirements of the model  
13 and limiting their applicability for detailed fault risk assessment. Moreover, faults and damage  
14 zones are significantly smaller than the grid cells employed in typical field-scale simulations  
15 necessitating either fine-scale gridding or local grid refinement around the fault zone to resolve  
16 their behaviour. While several workflows with detailed models that incorporate complex fault  
17 geometries, rock properties, explicitly gridded overlying formations and multiphase flow  
18 dynamics to capture the interplay between CO<sub>2</sub> migration, leakage, and pressure changes, the  
19 computational demands associated with such models can be prohibitive (Fachri et al., 2013, Jha  
20 and Juanes, 2014; Gasda et al., 2022; Snippe et al., 2022; Silva et al., 2023; Bjornara et al.,  
21 2023). This is especially true when considering uncertainties in subsurface data and the need  
22 for multiple simulations (scenario analyses) (Ringrose and Bentley, 2021). Sub-seismic faults,  
23 which are undetectable in seismic data, exacerbate modelling uncertainties due to their poorly  
24 constrained geometry, permeability, and potential connectivity (Yielding et al., 2007, Childs et  
25 al., 2009). Reservoir modelling to account for such complexities requires days to weeks to run,

1 limiting its utilization for early-stage site screening. These limitations underscore the urgent  
2 need for fast and efficient modelling tools that can evaluate fault-related leakage risks, support  
3 site selection, and identify risk mitigation strategies and monitoring plans in CCS projects. To  
4 address these limitations, this study introduces a simplified analytical fault leakage function  
5 that captures vertical flow dynamics within fault zones while avoiding the computational costs  
6 associated with explicit fault gridding or fine-scale modelling. The approach is explicitly  
7 designed for screening as it identifies which fault parameters and geological scenarios warrant  
8 detailed investigation, rather than attempting to forecast fault mechanisms.

9 Vertical equilibrium (VE) models have been developed to simplify three-dimensional  
10 multiphase flow simulations by leveraging two key characteristics of CO<sub>2</sub> storage systems: the  
11 strong buoyancy of CO<sub>2</sub> relative to brine and the significantly larger horizontal dimensions  
12 compared to the vertical dimension of the reservoir (Huppert and Woods, 1995; Yortsos, 1995;  
13 Nordbotten and Celia, 2011). These characteristics promote rapid CO<sub>2</sub> separation and vertical  
14 equilibrium within the reservoir. VE flow models exploit this phenomenon by enabling the  
15 representation of the 3D reservoir system using a set of 2D governing equations, thereby  
16 significantly reducing computational costs. Several CO<sub>2</sub> storage studies have demonstrated that  
17 VE simulations yield results comparable to those obtained from 3D simulations for benchmark  
18 and field-scale problems (Class et al., 2009; Nilsen et al., 2014; Bandilla et al., 2014; Nilsen et  
19 al., 2015; Nilsen et al., 2016; Moyner & Nilsen, 2019). The basic formulation of VE models  
20 assumes a sharp interface between CO<sub>2</sub> and brine and keeps the mathematical structure of the  
21 standard multi-phase Darcy equation. Hence, conventional simulators can be used. This very  
22 characteristic allows for their expansion to encompass a wider range of complex phenomena.  
23 Recent research has successfully incorporated and evaluated various physical effects within VE  
24 models, including: 1) capillarity – the presence of non-negligible capillary pressure leads to the  
25 formation of a capillary fringe, a transition zone between the CO<sub>2</sub> and brine phases, rather than

1 a sharp interface (Nordbotten & Dahle, 2011, Nilsen 2015); 2) residual trapping and hysteresis  
2 – these intrinsic properties of the rock can significantly influence the distribution and flow of  
3 fluids within the reservoir (Nordbotten & Celia, 2011; Doster et al., 2012; Doster et al., 2013;  
4 Du Plessis et al., 2013 Nilsen et al., 2016); 3) dissolution of CO<sub>2</sub> into reservoir brine (Gasda et  
5 al., 2011; Nilsen et al., 2016); 4) compressibility of CO<sub>2</sub> in the vertical extent (Andersen et al.,  
6 2015); 5) thermal effects (Gasda et al., 2013); 6) simplified geomechanics (Bjornara et al., 2016;  
7 Andersen et al., 2016, 2017); 7) Hybrid-VE – using a coupled approach of mixing 3D and VE  
8 models which can help with simulating near-wellbore effects and multilayer reservoir  
9 modelling (Moyner & Nilsen., 2019; Becker et al., 2017, 2018, 2022). These advancements  
10 have demonstrated the ability of VE models to capture complex dynamics with comparable  
11 accuracy to 3D simulations, making them a suitable approach for computationally efficient  
12 assessment of field-scale CO<sub>2</sub> storage, especially for early-stage projects which are subject to  
13 data uncertainty.

14 This study builds on these advancements by coupling a VE reservoir model with a newly  
15 developed fault leakage function to simulate vertical flow effects in faulted geological settings.  
16 We employ a VE flow model implemented within the open-source software package MRST-  
17 co2lab, which is a module within the MATLAB Reservoir Simulation Toolkit (MRST)  
18 (Andersen, 2017; Lie, 2019). The fault is conceptualized as an increased vertical permeability  
19 through the caprock (due to the fracture network in the damage zone) while the horizontal  
20 permeability is reduced (due to throw and the presence of the fault core). Leakage rates are  
21 estimated using Darcy's law, considering the pressure differential across the layers connected  
22 by the fault. The flow is modelled as vertical single-phase flow along the fault. This  
23 simplification allows for a one-dimensional leakage system which lowers the cost of  
24 computation. The mathematical formulation of the proposed model is presented in section 2,

1 and the results are discussed in section 3. The proposed modelling approach is demonstrated  
2 across four simulation cases presented in the results section.

3         The first case shows the verification of the upscaled fault leakage function against  
4 numerical simulations with explicitly gridded faults, demonstrating its accuracy in predicting  
5 along-fault leakage rates under varying fault permeability and capillary entry pressure  
6 conditions. The second case evaluates the model's robustness through convergence analysis  
7 across different grid resolutions and time step sizes, confirming its stability. The third case  
8 investigates the impact of capillary entry pressure using a sloping reservoir scenario, showing  
9 how increased capillary entry pressure delays leakage and reduces cumulative leakage rates.  
10 Finally, the model is applied to a field-scale CCS scenario in the Malay Basin, highlighting its  
11 efficiency and relevance for real-world fault leakage risk assessment.

## 12 2 Methods

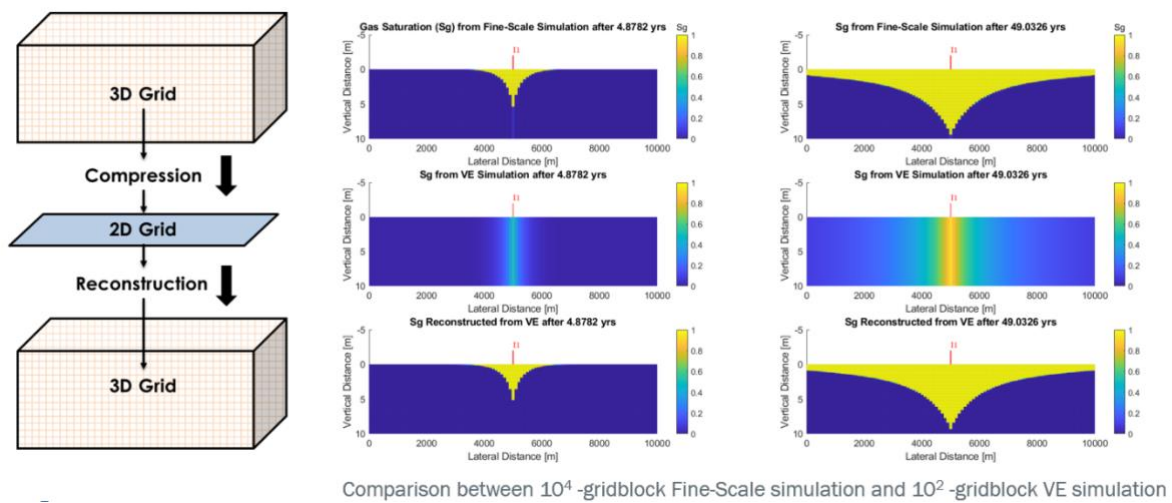
13         This study examines the potential for  $\text{CO}_2$  storage within a faulted reservoir (Figure  
14 1). We employ a vertically integrated numerical model for reservoir-scale flow coupled with an  
15 analytical model for fault leakage. A brief overview of the governing equations used in these  
16 models is presented in this section.

### 17 2.1 Vertical equilibrium modelling

18         The VE modelling approach for  $\text{CO}_2$  storage is a simplification of traditional reservoir  
19 simulation methods that is particularly useful for large-scale  $\text{CO}_2$  storage projects. This  
20 approach hinges on the assumption of VE, which posits that the buoyancy forces acting on the  
21  $\text{CO}_2$  cause it to segregate vertically much faster than it can migrate laterally. As a result, the  
22  $\text{CO}_2$  forms a thin layer beneath the caprock or under intermediate sealing layers, and the vertical  
23 pressure and fluid saturation distributions can be approximated by buoyancy and capillary  
24 forces. VE models reduce the dimensionality of the problem by vertically averaging the  
25 governing equations, which include conservation of mass and Darcy's law for fluid flow

1 through porous media. This simplification results in a model that requires fewer grid cells and  
 2 is computationally less intensive compared to full three-dimensional simulations. Post-  
 3 simulation, the vertical pressure and fluid saturations can be reconstructed from the set of  
 4 upscaled variables obtained by vertically integrating the conservation equations. Figure 2  
 5 illustrates the typical compression and reconstruction steps during a VE simulation at early and  
 6 late times for an example simulation problem. This section provides a concise review of  
 7 established equations for modelling flow in porous media and the VE simplification approach.  
 8 For a more general and in-depth treatment of the derivations and the limits of the VE  
 9 assumption, we refer the reader to the relevant literature (Yortsos 1995; Nordbotten & Celia,  
 10 2011).

11



12

13 Figure 2 – Illustration of the concept of VE model compression and reconstruction in a CO<sub>2</sub>  
 14 injection simulation. The top panel shows an illustrative representation of the 3D simulation  
 15 grid. The middle panel depicts the corresponding 2D grid generated by VE compression. The  
 16 bottom panel presents the reconstructed 3D simulation grid obtained by solving the 2D VE  
 17 model equations. These panels show the grid configuration at both early and late stages of the  
 18 CO<sub>2</sub> injection simulation. In this example, the VE compression reduces a  $10^4$ -cell 3D grid to a  
 19  $10^2$ -cell VE grid, achieving significant computational efficiency without substantial  
 20 information loss.

21

22 Consider the three-dimensional mass conservation equation for two immiscible and  
 23 incompressible fluid phases  $\alpha$ , CO<sub>2</sub> ( $\alpha = g$ ) and brine ( $\alpha = w$ ) as

$$\frac{\partial(\phi s_\alpha)}{\partial t} + \nabla \cdot \mathbf{u}_\alpha = q_\alpha, \quad (1)$$

1 where  $\phi$  is the porosity,  $s_\alpha$  is the saturation of phase  $\alpha$ ,  $\mathbf{u}_\alpha$  is the Darcy velocity of phase  $\alpha$ ,  
 2 and  $q_\alpha$  is a source/sink term in units of volume of phase  $\alpha$  per time. The porous medium is  
 3 assumed to be rigid and under isothermal conditions. The volume balance is established by

$$s_g + s_w = 1. \quad (2)$$

4 The Darcy velocity of each phase is given by

$$\mathbf{u}_\alpha = -\frac{k_{r\alpha}}{\mu_\alpha} \mathbf{k}(\nabla p_\alpha - \rho_\alpha \mathbf{g}), \quad (3)$$

5 where  $\mu_\alpha$  is the viscosity of phase  $\alpha$ ,  $k_{r\alpha}$  is the relative permeability of phase  $\alpha$ ,  $\mathbf{k}$  is the  
 6 permeability tensor,  $p_\alpha$  is the fluid pressure of phase  $\alpha$ ,  $\rho_\alpha$  is the density of phase  $\alpha$ , and  $\mathbf{g}$  is  
 7 the gravity acceleration vector. The phase pressures are related by the capillary pressure  
 8 function

$$p_c = p_g - p_w. \quad (4)$$

9 It is also assumed that the capillary pressure and relative permeability can be represented  
 10 by algebraic functions. These functions depend solely on saturation and its history. Equations  
 11 (1) to (4) form a set of 10 equations with 10 unknowns that need to be solved for in three  
 12 dimensions. The fluid saturation distributions and pressures are obtained by solving this system,  
 13 provided that: 1) specific functions are chosen to represent relative permeability and capillary  
 14 pressure, 2) initial conditions for pressure and saturation throughout the reservoir are provided,  
 15 and 3) appropriate boundary conditions are specified along the edges of the reservoir model.

16 In subsurface flow processes, the lateral dimension of interest is typically orders of  
 17 magnitude larger (hundreds of meters to kilometers) compared to the vertical dimension (meters  
 18 to tens of meters). This disparity leads to a more rapid redistribution of fluids vertically,  
 19 allowing for the approximation of VE (Nordbotten & Celia, 2011; Nordbotten & Dahle, 2011).  
 20 Consider a reservoir domain bounded by impermeable, horizontally oriented layers with a

1 constant thickness  $H$ . The two fluids (brine and  $\text{CO}_2$ ) are separated by a sharp interface within  
2 this reservoir. A cartesian coordinate system is employed, with the  $z$ -axis oriented in opposition  
3 to the gravitational vector (positive  $z$  upwards). Furthermore, for simplicity in the presentation  
4 here, constant permeability and porosity are assumed within the vertical direction, though VE  
5 is not limited to those assumptions (Nordbotten & Celia 2012).

6 This vertical integration seeks to establish governing equations for the horizontal plane  
7 that utilize variables representing the average behaviour throughout the reservoir thickness.  
8 Fine-scale quantities capture variations within the vertical dimension, while coarse-scale  
9 quantities represent the horizontally averaged behaviour. Under the assumption of vertical  
10 hydrostatic equilibrium, Equation (3) indicates that the pressure gradient in each phase balances  
11 the gravity ( $u_{\alpha z} = 0$ ). This characteristic allows for the determination of pressure at any vertical  
12 position by integrating the pressure from a reference level. To facilitate analysis, we normalize  
13 the  $z$ -axis with respect to the reservoir height  $H$ . Here,  $z = 0$  is assigned to the bottom and  $z =$   
14  $1$  to the top of the reservoir. Consequently, the top of the reservoir is chosen as the reference  
15 position for pressure integration as

$$P_\alpha = p_\alpha(z = 1). \quad (5)$$

16 The reconstructed pressure is then given as

$$p_\alpha(z) = P_\alpha + \rho_\alpha g H (1 - z). \quad (6)$$

17 The other coarse-scale quantities are introduced by integrating the fine-scale quantities.  
18 This is done under the assumption of a homogeneous system with isothermal and  
19 incompressible fluids. We can obtain the coarse-scale equivalents after normalizing the vertical  
20 axis to the reservoir height and writing the equations in dimensionless form. For such systems,  
21 the coarse-scale equivalents of porosity  $\Phi$ , permeability  $K$ , and viscosity  $M_\alpha$  are simply a  
22 product of their respective fine-scale counterparts with reservoir height. This is because the

1 averaging or integration process does not introduce any scaling factors in this case. The spatially  
 2 dependent quantities are given as

$$S_\alpha = \frac{H}{\Phi} \int_0^1 \phi s_\alpha dz, \quad (7)$$

$$U_\alpha = H \int_0^1 u_{\alpha||} dz, \quad (8)$$

$$K_{r\alpha} = \frac{H}{K} \int_0^1 k_{||} k_{r\alpha}(s_\alpha(z)) dz. \quad (9)$$

3 The subscript  $||$  denotes the variables in horizontal components such that  $U_\alpha$  is a two-  
 4 dimensional vector instead of three dimensions. With these definitions, Equations (1) to (4)  
 5 after integrating over the vertical extent are given as

$$\frac{\partial(\Phi S_\alpha)}{\partial t} + \nabla_{||} \cdot (U_\alpha) = Q_\alpha, \quad (10)$$

$$S_g + S_w = 1, \quad (11)$$

$$U_\alpha = -K \frac{K_{r\alpha}}{M_\alpha} \nabla_{||} P_\alpha, \quad (12)$$

$$P_c(\bullet) = P_g - P_w, \quad (13)$$

6 where  $(\bullet)$  is used to highlight the upscaled dependence of the capillary pressure function that is  
 7 yet to be determined. Equation (9) demonstrates that reconstructing the vertical, fine-scale  
 8 saturation distributions,  $s_w(z; x, y)$ , is necessary to determine the effective parameter functions  
 9 employed in a purely coarse-scale model. Fortunately, the assumption of hydrostatic fluid  
 10 distribution facilitates this reconstruction process. By examining Equation (6), we observe that  
 11 the fine-scale capillary pressure,  $p_c(z; x, y)$ , must compensate for the buoyancy force arising  
 12 from the density difference. This relationship allows for the construction of the fine-scale  
 13 capillary pressure and its subsequent connection to the coarse-scale capillary pressure as

$$p_c(z; x, y) = P_c(x, y) - (\rho_w - \rho_g)gH(1 - z). \quad (14)$$

1           A well-defined relationship between capillary pressure and water saturation enables the  
2 establishment of invertible  $p_c - s_w$  mappings. These mappings allow for the reconstruction of  
3 the vertical saturation distribution,  $s_w(z; x, y)$ , given a specific coarse-scale capillary pressure  
4  $P_c$ . Furthermore, Equation (7) can be employed to obtain a  $P_c - S_w$  relationship. By leveraging  
5 this relationship, the fine-scale saturation distribution  $s_w(z; x, y)$  is determined for a given  
6 coarse-scale saturation  $S_w$ . Consequently, coarse-scale relative permeabilities  $K_{r\alpha}$  are  
7 dependent on coarse-scale saturations only.

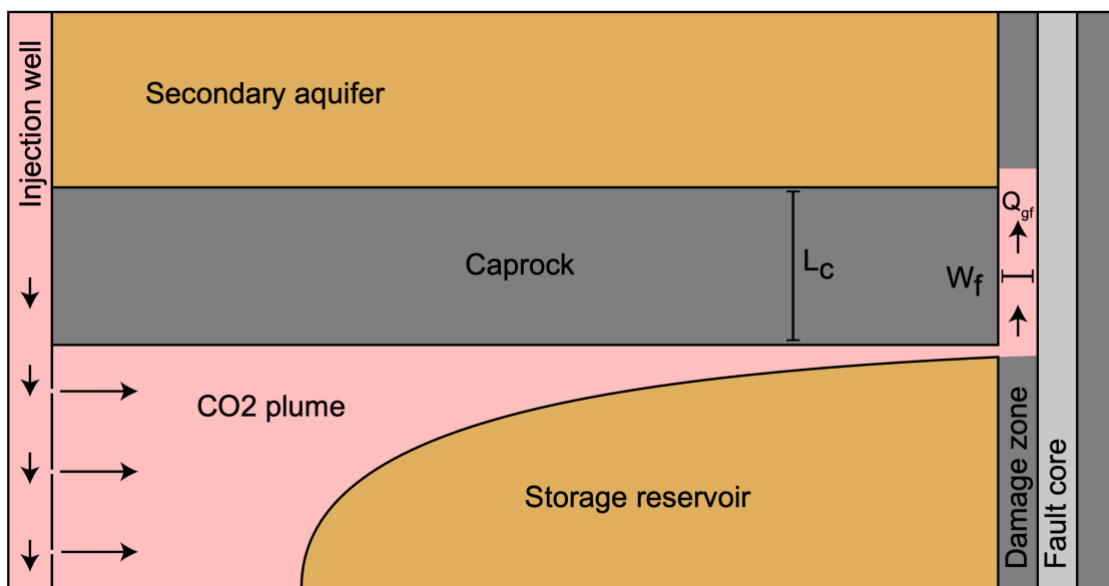
## 8 2.2 Fault leakage function

9           This section details the steady-state analytical solution used to estimate leakage rates  
10 along the fault. The fault is conceptualized to connect the storage reservoir with a secondary  
11 aquifer at a shallower depth, which acts as sink for the leaking CO<sub>2</sub>. Only faults of shorter  
12 lengths such that the CO<sub>2</sub> fluid properties remain nearly constant are considered here, while the  
13 long-range fault leakage (faults that connect the reservoir to the surface or seafloor) with  
14 variable CO<sub>2</sub> fluid properties and decompressive cooling has been investigated previously  
15 (Pruess, 2011; Ramachandran et al., 2017). The leaky fault is conceptualized as consisting of a  
16 low-conductivity (i.e., low permeability) core that could prevent flow across the fault. This core  
17 is surrounded by two high-conductivity (i.e., high-permeability) damage zones that permit flow  
18 vertically along the fault as shown in Figure 3 (Faulkner et al., 2010). This damage zone is  
19 referred to here as "the fault zone" or simply "the fault". This zone contains a low conductivity  
20 core that typically extends vertically into the reservoir. In this conceptualization, for the sake  
21 of simplicity, the flow across this low-conductivity core is represented as a no-flow boundary.  
22 However, it is important to note that flow across the core is typically represented using  
23 transmissibility multipliers (Manzocchi et al., 1999). Therefore, under this simplified no-flow  
24 assumption, fault leakage is conceptualized to occur upwards along the damage zone, which is  
25 modelled as an equivalent porous medium with representative rock properties.

1 This conceptualization embodies several key assumptions appropriate for early-stage screening  
2 but not for detailed site characterization. We assume the fault damage zone is pre-existing and  
3 permeable, with permeability treated as constant rather than being stress-dependent. We do not  
4 model fault reactivation or injection-induced permeability evolution, processes that have been  
5 shown to significantly influence fault behaviour and leakage dynamics during CO<sub>2</sub> injection  
6 (Rinaldi et al., 2014; Jha and Juanes, 2014; Rutqvist, 2012; Vilarrasa et al., 2017). These  
7 assumptions are appropriate for screening analyses evaluating scenarios where permeable  
8 pathways are assumed to exist. They are not appropriate for predicting whether faults will  
9 reactivate or for sites where critically stressed faults near failure are the primary concern for  
10 which coupled geomechanical-dynamic models are required (Chang and Segall, 2016; Zhao  
11 and Jha, 2019; Meguerdijian and Jha, 2021). The simplifications enable computational  
12 efficiency necessary for evaluating multiple sites and uncertainty realizations during initial  
13 screening, when detailed geomechanical data is unavailable and the goal is identifying sites  
14 warranting further investigation. This approach further allows exploration of fault  
15 permeabilities that lead to significant leakage and guides site prioritization for detailed  
16 assessment.

17 Estimating the hydraulic properties of the fault, particularly within the fault core and damage  
18 zone, is crucial for accurately modelling fault leakage. Fault zone permeabilities exhibit  
19 considerable variability depending on fault architecture, lithology, stress state, and deformation  
20 history. Fault zone permeabilities can range over ten orders of magnitude, from  $10^{-9}$  to  $10^{-19}$  m<sup>2</sup>  
21 (Childs et al., 2009; Faulkner et al., 2010), with strong contrasts between different fault  
22 components. Specifically, fault cores exhibit relatively low permeability ( $10^{-17}$  to  $10^{-21}$  m<sup>2</sup>) due  
23 to cataclasis, clay smear, and gouge formation (Bense and Person, 2006; Rinaldi et al., 2014).  
24 In contrast, damage zones are typically several orders of magnitude more permeable and  
25 strongly depends on the nature of well-connected fracture networks (Caine et al., 1996;

1 Faulkner et al., 2010; Rizzo et al., 2024). While insights can be gained from studying outcrop  
 2 analogues, inherent uncertainties remain at the finer scale. Several researchers have developed  
 3 stochastic modelling approaches to predict the fault properties, such as permeability, among  
 4 other parameters (Berge et al., 2022; Gasda et al., 2022; Salo-Salgado et al., 2023; Rizzo et al.,  
 5 2024; Pettersson et al., 2025). However, for this specific model, we are assuming constant fault  
 6 properties throughout the simulation. The flow along the fault is described using Darcy's law  
 7 by considering the pressure differential across the storage reservoir and the secondary aquifer,  
 8 and the flow is assumed to occur only in the vertical direction. Once the CO<sub>2</sub> plume reaches the  
 9 base of the fault within the aquifer, it is hypothesized to form a thick layer, acting as a barrier  
 10 for aqueous phase entry into the fault (Kang et al., 2014). As a result, the aqueous flux along  
 11 the fault is considered negligible and excluded from the function.



12  
 13 Figure 3 – A schematic representation of a vertical cross-section of a storage reservoir  
 14 containing a fault (gray). The black line represents the interface between the CO<sub>2</sub> and brine  
 15 phases. CO<sub>2</sub> leaks along the damage zone of the fault after reaching the base of the fault within  
 16 the reservoir.

17  
 18 Several researchers have indicated that the CO<sub>2</sub> needs to overcome the capillary entry  
 19 pressure of the fault, commonly referred to as the fault displacement pressure, for it to leak  
 20 (Espinoza et al., 2017; Zheng & Espinoza, 2022). Fault capillary entry pressure depends on

1 effective fracture aperture, wettability, and stress conditions. For intact caprocks, breakthrough  
 2 pressures typically range from 0.5 to 5 MPa depending on lithology (Espinoza et al., 2017).  
 3 However, fault damage zones with open fractures typically exhibit significantly lower entry  
 4 pressures reflecting the larger effective apertures of fracture networks (Zheng and Espinoza,  
 5 2022; Snippe et al., 2022). For simplicity, we keep this parameter constant here. We base the  
 6 flux calculation on the model presented by Neufeld et al. (2009) and Gilmore et al., (2022),  
 7 with slight modifications to account for the reservoir overpressure caused by injection. This  
 8 model describes leakage through fissures between two aquifers, with one being the targeted  
 9 CO<sub>2</sub> storage site. We model the driving potentials  $\psi$  as

$$\psi = \Delta\rho gh_g + (P_w - P_{w0}) - p_e, \quad (15)$$

10 where  $\Delta\rho = \rho_w - \rho_g$  is the density difference between brine and CO<sub>2</sub>,  $h_g$  is the height of CO<sub>2</sub>  
 11 which is obtained from the coarse-scale gas saturation  $S_g$  (after accounting for the reservoir  
 12 rock-fluid characteristics), of the reservoir block connected to the fault block,  $P_w$  is the brine  
 13 pressure in the reservoir,  $P_{w0}$  is the initial brine pressure in the reservoir, and  $p_e$  is the capillary  
 14 entry pressure of the fault/fractures. The vertical gas leakage flux  $Q_{gf}$  along the fault is given  
 15 as

$$Q_{gf} = \begin{cases} 0, & \psi \leq 0 \\ \frac{A_f k_f (\psi + \Delta\rho g L_c)}{\mu_g L_c}, & \psi > 0 \end{cases}, \quad (16)$$

16 where  $A_f$  is the area of the fault perpendicular to flow,  $k_f$  is the vertical fault permeability and  
 17  $L_c$  is length of the caprock or the length of the fault connecting the reservoir to the secondary  
 18 aquifer. This formulation accounts for the capillary entry pressure required for CO<sub>2</sub> to enter the  
 19 fault. This approach relaxes the assumption of VE at the grid block where the fault is connected,  
 20 allowing for non-zero vertical flow. However, for steady state single phase flow, fault leakage  
 21 does not have a significant effect on reservoir predictions (Kang et al., 2014). By incorporating

1 these key factors, the function aims to provide a more realistic representation of the fault  
2 leakage process.

### 3 2.3 Model implementation

4 The leakage along the fault is numerically simulated as a fault leakage function, which  
5 is represented as a source/sink term in the material balance equations (Equation 10). This  
6 methodology circumvents the explicit discretization of faults, thereby capturing their impact on  
7 fluid flow and replicating their influence without requiring a computationally intensive, fully  
8 discretized fault representation. The fault leakage function is related implicitly to the primary  
9 unknowns of the reservoir model using the gas saturation and the overpressure terms of the grid  
10 blocks adjacent to the fault. The flow rate at the fault-reservoir interface is represented as shown  
11 in Equation 16. From a simulation perspective, fault leakage occurs when the leakage  
12 constraint, expressed as  $\Delta\rho gh_g + (P_w - P_{w0})$ , exceeds the fault capillary entry pressure  $p_e$  and  
13 the upscaled gas saturation is greater than zero. However, numerical experiments have  
14 demonstrated that this criterion can result in unstable behaviour, characterized by frequent  
15 fluctuations (appearance and disappearance of the fault leakage term) during the iteration  
16 process and between time steps, which causes convergence issues and increased simulation  
17 time. To address this problem, the implementation of a smoothing function for the leakage rate  
18 term enables a more robust fault leakage function. We use a smoothing function, such that  
19  $\hat{Q}_{gf} = Q_{gf}f(\psi)$  with the smoothing function  $f(\psi) = (1 - e^{(-\xi\psi)})$  and the smoothing  
20 parameter  $\xi$ . In our simulations we use  $\xi = 10^{-3} Pa^{-1}$  to regulate the fault leakage rate upon  
21 the initial occurrence of a non-zero fault leakage term. Under rigorous consideration, permitting  
22 the leakage constraint to marginally exceed  $p_e$  without initiating fault leakage introduces a  
23 minor inaccuracy in leakage rates. However, this approach has a negligible impact on long-term  
24 simulation results while significantly improving the efficiency of the simulations with respect  
25 to timesteps and convergence. The fault permeability assigned to the fault leakage term

1 represents the vertical permeability of the damage zone only. The fault core is treated as  
2 impermeable, preventing across-fault flow, while the damage zone acts as the vertical conduit  
3 for CO<sub>2</sub> leakage to overlying formations. The resulting reservoir is discretized based on a finite  
4 volume discretization using the two-point flux approximation method, as implemented in the  
5 MRST (Lie, 2019) framework.

## 6 3 Results

7 In this section, we present the results obtained from applying the fault leakage function  
8 coupled with the VE reservoir model to several CO<sub>2</sub> injection scenarios.

### 9 3.1 Case 1 – Comparison with 2D simulations

10 The cases presented in this section are designed to verify our upscaled fault leakage  
11 function accurately reproduces the flow behaviour of an explicitly gridded fault system. A 2D  
12 two-phase numerical model is used to simulate the fault leakage rates within the simplified CO<sub>2</sub>  
13 storage setting (Figure 4a). The objective of this case is to compare the fault leakage rates  
14 between the 2D numerical simulation with an explicit representation of the fault and the VE  
15 model with the fault leakage function proposed in this work. This case simulates fluid flow  
16 through a conceptual model comprising two horizontal aquifers separated by a caprock and  
17 connected by a vertical, conductive fault. The fault is treated as an equivalent porous medium  
18 with the reservoir, fault, fluid, and rock-fluid properties as specified in Table 1. Although the  
19 permeability of the aquifers and faults is simplified for comparative purposes, it is crucial to  
20 emphasize that the primary focus is on the interaction of these components, rather than precise  
21 geological representation.

22 A numerical grid of 12,000 cells discretizes the system with a resolution of 1 m x 1 m x  
23 0.25 m (in the x, y, and z directions, respectively), resulting in a physical model with dimensions  
24 of 100 m x 30 m, consisting of three layers, each 10 m thick. The fault zone, located on the  
25 right side of the model, is 5 m wide and 10 m long. The system is assumed to be in hydrostatic

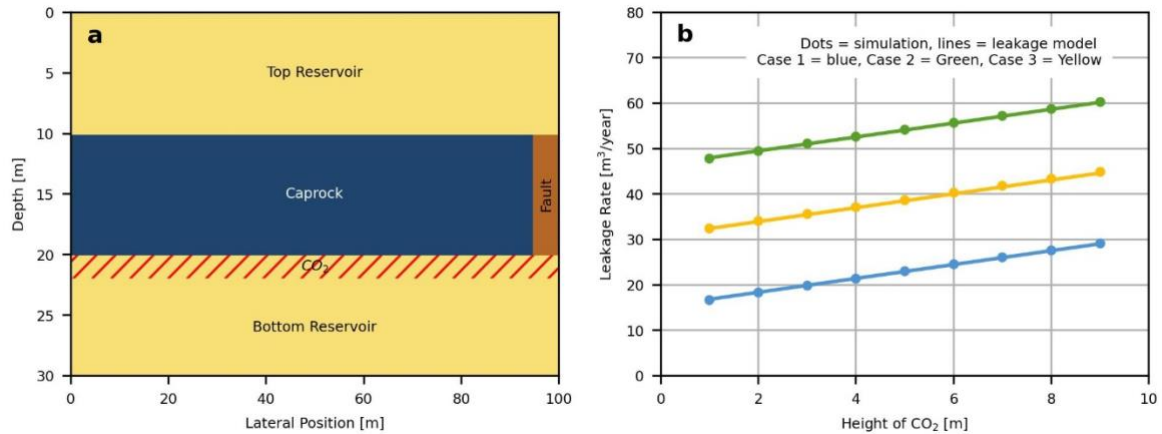
1 equilibrium with 100% water saturation initially, and the relative permeability is governed by  
2 the Brooks-Corey model with parameters described in Table 1. No-flow boundaries are  
3 assumed at the top, bottom, and the right side (representing no flow across the fault core). The  
4 left boundary is treated as an open boundary, with the pressure maintained as hydrostatic. The  
5 system is initialized with a constant CO<sub>2</sub> column height at the left boundary of the storage  
6 reservoir. This column height and the boundary pressures can be varied to simulate buoyancy-  
7 driven and pressure-driven conditions, allowing for a comprehensive evaluation of the fault  
8 leakage modelling approach.

9  
10 Table 1 – Summary of model parameters used for fault leakage function verification simulation  
11 described in section 3.1.

Property	Value
<b>Bottom Reservoir and Top Reservoir Properties</b>	
Top reservoir porosity	0.3
Bottom reservoir porosity	0.3
Top reservoir permeability (mD)	100
Bottom reservoir permeability (mD)	100
Reservoir overpressure (bars) (case 2 and 3)	1
<b>Caprock properties</b>	
Caprock permeability (mD)	$1 \times 10^{-6}$
Caprock porosity	0.05
<b>Fault damage zone properties</b>	
Fault damage zone porosity	0.03
Fault damage zone permeability (mD)	1
Fault damage zone width (m)	5
Fault damage zone length (m)	10
Fault damage zone capillary entry pressure (bars) (case 3)	0.5
<b>Bottom Reservoir, Fault and Top Reservoir Relative Permeability Properties</b>	
Residual gas saturation	0
Residual brine saturation	0
Gas end-point relative permeability	1
Brine end-point relative permeability	1
Gas relative permeability exponent	1
Brine relative permeability exponent	1
<b>Fluid properties</b>	
Gas density (kgm <sup>-3</sup> )	500
Brine density (kgm <sup>-3</sup> )	1000
Gas viscosity (Pa.s)	$5 \times 10^{-5}$
Brine viscosity (Pa.s)	$3.13 \times 10^{-4}$

1            Three specific parametrizations are considered to compare the performance of the fault  
2 leakage modelling approach, 1) The reservoir and boundary pressures are hydrostatic. The  
3 pressure of the CO<sub>2</sub> column is derived solely from density differences, and the flow is driven  
4 by buoyancy. This parametrization mimics the migration phase of CO<sub>2</sub> storage. 2) The reservoir  
5 pressure is hydrostatic, but the boundary pressure is elevated to mimic the typical pressure  
6 increase observed during injection. The pressure of the CO<sub>2</sub> column is derived from both the  
7 density differences, and the pressure elevation. 3) Similar to Case 2, the third scenario contains  
8 an additional capillary entry pressure for the fault, which acts as a pressure barrier that the CO<sub>2</sub>  
9 must exceed to enter the fault zone. The 2D numerical simulations are run to steady-state  
10 conditions for each of the three cases. The leakage rate, specified as the flow leaving from the  
11 top of the fault, is then compared to the leakage rate obtained from the VE model with the fault  
12 leakage function (Figure 4b). The proposed fault leakage function shows excellent agreement  
13 with numerical simulations with explicitly gridded faults for all three scenarios. This  
14 demonstrates that it is suitable for capturing the same flow physics influencing fault-related  
15 CO<sub>2</sub> leakage, i.e., buoyancy, pressure gradients, and capillary entry pressure. Moreover, the  
16 model's computational efficiency is improved by bypassing the explicit representation of the  
17 fault and top reservoir. This verification gives confidence that our model can be applied to field-  
18 scale CO<sub>2</sub> storage simulations.

19



1  
 2 Figure 4 –Grid representation of 2-D fine scale simulation (a) and fault leakage rate comparison  
 3 between numerical simulation and VE model with fault leakage function (b). The three cases  
 4 considered are: (1) hydrostatic reservoir and boundary pressure, (2) elevated reservoir boundary  
 5 pressure, and (3) fault capillary entry pressure.  
 6

7           It is important to highlight the potential limitations of the steady-state, single-phase fault  
 8 leakage assumption used in our modelling approach. For instance, in the overpressure  
 9 parametrization (2) with a 5-meter CO<sub>2</sub> column height, the calculated leakage rate is 53 m<sup>3</sup> per  
 10 year. Accounting for the fault dimensions, this corresponds to a CO<sub>2</sub> Darcy flux of 0.03 m per  
 11 day and the corresponding pore velocity of 1 m per day. This implies that it takes approximately  
 12 10 days, for the CO<sub>2</sub> to travel the 10-meter distance separating the bottom reservoir and the top  
 13 reservoir. Although faults are typically characterized by very low porosity, and the impact of  
 14 CO<sub>2</sub> accumulation within the fault on the leakage rate may be minimal (Faulkner et al., 2010;  
 15 Caine et al., 1996), there remains a delay in reaching the top reservoir that is not captured,  
 16 because the current approach presupposes instantaneous leakage once the CO<sub>2</sub> reaches the base  
 17 of the fault. This raises a pertinent question regarding the definition of leakage - whether it  
 18 occurs once CO<sub>2</sub> enters the top reservoir or once it enters the fault from the bottom reservoir.  
 19 However, the current modelling approach does not explicitly account for these dynamic effects  
 20 during the fault leakage process. While acknowledging these limitations is crucial, it is equally  
 21 important to contextualize the scale of typical CO<sub>2</sub> storage simulations, which extend from a

1 few decades to a few centuries. Within this broader temporal framework, the steady-state,  
2 single-phase assumption may offer a reasonable approximation that allows us to screen leakage  
3 rates across a broad range of possible reservoir scenarios before commencing more detailed  
4 simulation studies that capture the full physics of fault leakage in a specific reservoir scenario.  
5 This consideration underscores the necessity of balancing model complexity with  
6 computational feasibility, particularly in the context of large-scale, long-term CO<sub>2</sub> storage  
7 simulations.

### 8 3.2 Case 2 - Convergence analysis

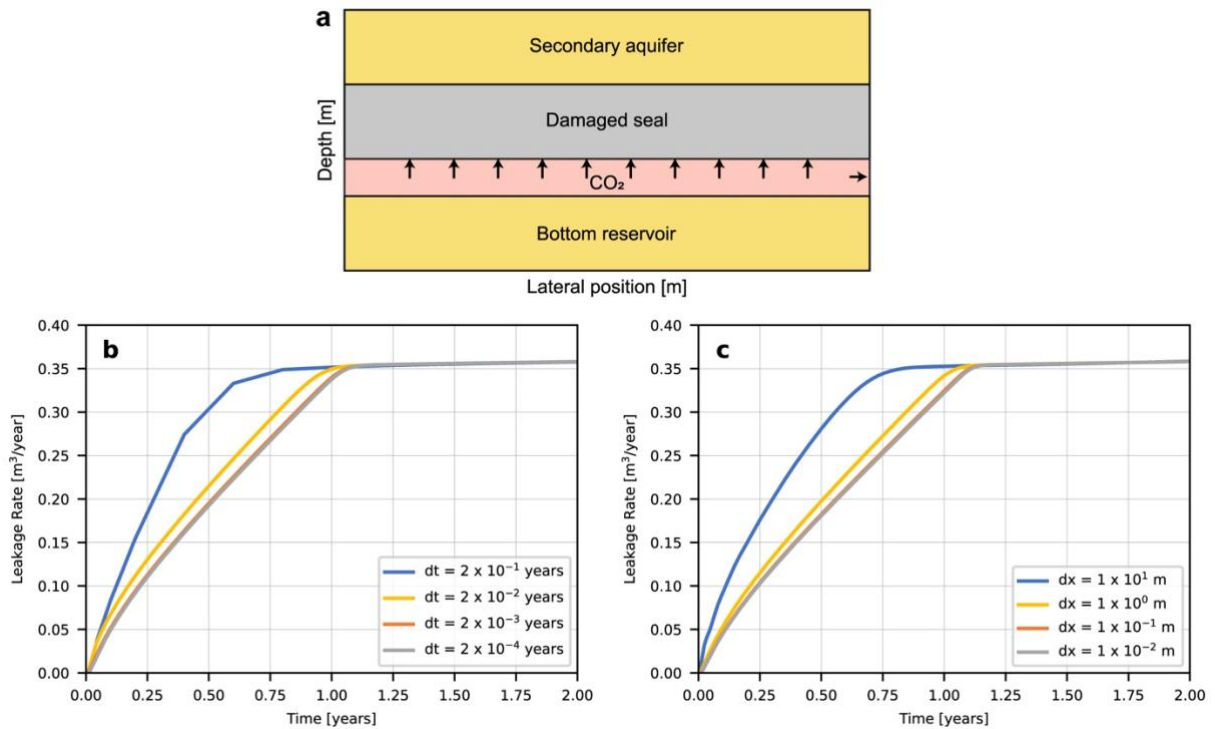
9         The following case aims to assess the impact of grid resolution and time step size on the  
10 fault leakage modelling methods presented in Section 2. A 2D, two-phase numerical model is  
11 employed to simulate leakage rates within a simplified CO<sub>2</sub> storage setting (Figure 5a). This  
12 case, with minor modifications, is based on the scenario described in Section 3.1. It simulates  
13 fluid flow through a geological model consisting of a horizontal aquifer located beneath a  
14 damaged seal, which behaves like a damage zone from the previous case. There is no fault core  
15 in this case. In this model, the caprock is replaced with a damaged seal, which is represented as  
16 a continuous leakage pathway, allowing any CO<sub>2</sub> accumulated beneath it to migrate upward  
17 and leak into a secondary aquifer. This seal extends horizontally across the reservoir and  
18 vertically into overlying strata, thereby hydraulically connecting the storage reservoir to a  
19 secondary aquifer. CO<sub>2</sub> leakage is quantified at the interface between the damaged seal and the  
20 secondary aquifer. To capture this vertical migration, the grid cells encompassing the damaged  
21 seal employ the fault leakage function and associated parameters specified in Table 2. The  
22 aquifer serves as the storage reservoir, and the damaged seal is treated as an equivalent porous  
23 medium. The properties of the reservoir, damaged seal, fluid, and rock-fluid interactions are  
24 specified in Table 2. For the purposes of testing numerical convergence and stability, we  
25 adopted simplified physical dimensions for both the aquifer and damaged seal (100 m wide and

1 10 m long). The objective of this case is to demonstrate that our implementation produces  
2 stable, converged solutions across different grid resolutions and time-step sizes. The system is  
3 assumed to be in hydrostatic equilibrium with an initial water saturation of 100%. Relative  
4 permeability is governed by the Brooks-Corey model, with parameters detailed in Table 2. No-  
5 flow boundaries are assumed at the top and bottom, while the left and right boundaries are  
6 treated as open, with pressure maintained as hydrostatic. The system is initialized with a  
7 constant CO<sub>2</sub> column height of 5 m at the left boundary of the storage reservoir. This column  
8 height and the boundary pressures can be varied to simulate buoyancy-driven and pressure-  
9 driven conditions, similar to those in Section 3.1. The grid blocks enclosing the damaged seal  
10 is modified to incorporate the fault leakage function, with properties mentioned in Table 2, to  
11 mimic along-fault leakage.

12 Table 2 – Summary of model parameters used for convergence analysis simulation described  
13 in section 3.2.

<b>Property</b>	<b>Value</b>
<b>Reservoir Properties</b>	
Reservoir porosity	0.3
Reservoir permeability (mD)	100
<b>Damaged seal properties</b>	
Damaged seal porosity	0.03
Damaged seal permeability (mD)	$1 \times 10^{-3}$
Damaged seal length (m)	10
<b>Reservoir and Damaged Seal Relative Permeability Properties</b>	
Residual gas saturation	0
Residual brine saturation	0
Gas end-point relative permeability	1
Brine end-point relative permeability	1
Gas relative permeability exponent	1
Brine relative permeability exponent	1
<b>Fluid properties</b>	
Gas density (kgm <sup>-3</sup> )	500
Brine density (kgm <sup>-3</sup> )	1000
Gas viscosity (Pa.s)	$5 \times 10^{-5}$
Brine viscosity (Pa.s)	$3.13 \times 10^{-4}$

1  
2



3 Figure 5 – Conceptual representation of VE simulation setup of CO<sub>2</sub> storage with a damaged  
4 seal to assess the impact of grid block dimensions and time step size on leakage modelling (a),  
5 leakage rate comparison for varying time step sizes for a constant grid block dimension of 1 m  
6 (b) and leakage rate comparison for varying gridblock dimensions at a time step of 4 x 10<sup>-3</sup>  
7 years (c).

8

9

Figure 5b illustrates the leakage rate for two years with time steps varying from 2 x 10<sup>-1</sup>  
10 years to 2 x 10<sup>-4</sup> years and a grid block dimension of 1 m. Figure 5c illustrates the leakage rate  
11 for two years with grid block dimensions varying from 1 x 10<sup>1</sup> m to 1 x 10<sup>-2</sup> m and a time step  
12 of 4 x 10<sup>-3</sup> years. A key observation is that the leakage rate converges towards a consistent  
13 solution for both, time and space. Coarser grids and larger time steps lead to overestimated  
14 leakage rates in the first year. Subsequently, all time steps and grid block sizes converge toward  
15 the same leakage rate predictions. While the total leakage increases with larger time steps and  
16 grid sizes, the magnitude of this increase becomes negligible after 100 years of simulation  
17 (when the system reaches steady state). For instance, the total leakage after 100 years is only  
18 0.0025% higher for the 2 x 10<sup>-1</sup> year time step compared to the 2 x 10<sup>-3</sup> year time step, and  
19 0.0027% higher for the 1 x 10<sup>1</sup> m grid size compared to the 1 x 10<sup>-2</sup> m grid size. Resizing grid

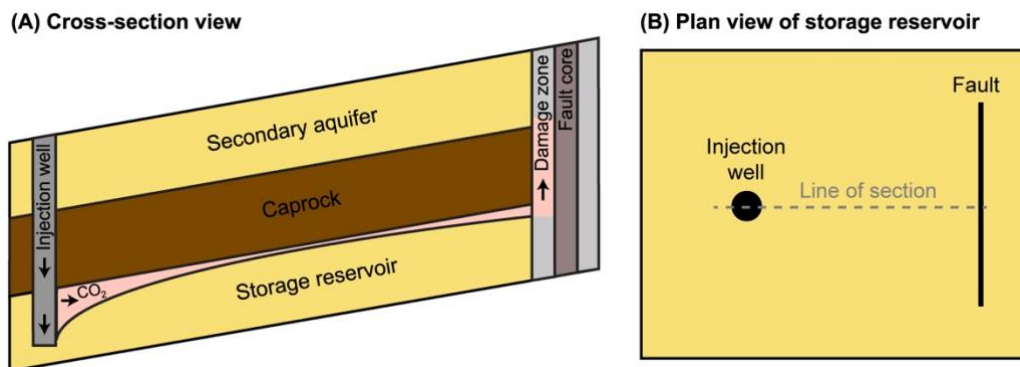
1 blocks proportionally resizes the fault leakage function, ensuring the total damaged seal width  
2 remains constant. Consequently, the number of leakage terms increases with a higher number  
3 of grid blocks. Despite this increase, the impact on total leakage predictions remains relatively  
4 low. It is important to acknowledge that this model uses a fault leakage function instead of  
5 explicitly representing the faults, to ensure computational efficiency. Despite this  
6 simplification, the model is able to approximate the reservoir behaviour and leakage rates  
7 outcomes with sufficient reliability. This approach facilitates the rapid screening of potential  
8 storage sites, enabling the identification of promising candidates. Consequently, resources can  
9 be strategically allocated to design comprehensive data acquisition campaigns tailored to the  
10 specific geological complexities of selected sites. By expediting the early screening phase, this  
11 methodology contributes to the overall acceleration of CO<sub>2</sub> storage project development in  
12 geologically complex settings.

### 13 3.3 Case 3 - Sloping reservoir with a leaky fault

14 The case presented in this section is designed to test the fault leakage function for a  
15 gently sloping reservoir with a large fault. The conceptual model comprising a gently sloping  
16 reservoir connected to a secondary aquifer by a fault is shown in Figure 6. The reservoir is  
17 discretized as a VE grid with 2500 cells, each measuring 20 m x 20 m in the x and y directions,  
18 respectively, resulting in a physical model with dimensions of 1000 m x 1000 m. The reservoir  
19 has a thickness of 10 m and a slope of ~3 degrees. The fault is treated as an equivalent porous  
20 medium using the fault function, and the reservoir, fault, fluid, and rock-fluid properties as  
21 specified in Table 3. The fault is positioned to intersect the reservoir and extend vertically into  
22 the caprock and hydraulically connect the storage reservoir to a secondary aquifer. Leakage is  
23 measured at the top of the fault (fault-secondary aquifer interface), capturing the rate of CO<sub>2</sub>  
24 exiting the storage reservoir along the fault. The grid blocks enclosing the fault are modified to  
25 1) set the across-fault permeability within the reservoir to zero, mimicking an impermeable

1 fault core, and 2) incorporate the fault leakage function with the properties mentioned in Table  
2 3 to mimic along fault leakage. The system is assumed to be in hydrostatic equilibrium with  
3 100% water saturation initially, and the relative permeability is governed by the Brooks-Corey  
4 model with parameters mentioned in Table 3. No-flow boundaries are assumed at the top, right  
5 and left boundaries of the VE reservoir. The bottom boundary is treated as an open boundary  
6 with the pressure maintained as hydrostatic. Hence this bottom boundary acts as a sink for the  
7 heavier brine phase and allows for up-dip movement of CO<sub>2</sub>. Unlike previous simulations where  
8 the CO<sub>2</sub> injection was controlled by boundary conditions, this simulation uses the rate  
9 constrained well for CO<sub>2</sub> injection. The injection location is at the coordinate pair (100 m, 500  
10 m) for an injection rate of 1229 tons per year over 3 years followed by 97 years of migration.  
11 The fault zone is located in the center of the model, i.e., 500 m away from either side boundary  
12 in x-direction as shown in Figure 7a. The fault is 800 m long in the y-direction. The goal of this  
13 case study is to analyse the evolution of CO<sub>2</sub> leakage rates and assess the impact of fault  
14 capillary entry pressure on these rates.

15



16

17

18 Figure 6 – The conceptual model showing a gently sloping reservoir connected to a secondary  
19 aquifer by a leaky fault in the cross-section view (a) and the reservoir in plan view (b).

20

21 VE reservoir simulation is conducted with a time step of one year to evaluate the impact  
22 of the fault on the migration of a CO<sub>2</sub> plume within the reservoir. The evolution of the CO<sub>2</sub>  
23 plume is depicted at the end of the injection period (Figure 7b) and after 97 years of migration

1 (Figure 7c). The simulation results demonstrate the preferential up-dip movement of the CO<sub>2</sub>  
2 plume within the reservoir. Notably, significant quantities of CO<sub>2</sub> are observed to accumulate  
3 at the base of the fault since the impermeable fault core inhibited further across-fault migration  
4 within the reservoir. This leads to an increase in gas saturation down dip of the fault until the  
5 CO<sub>2</sub> plume migrated laterally to the fault tips, after which it continued its unhindered up-dip  
6 movement. Leakage along the fault occurs once the CO<sub>2</sub> reached the fault. The leakage rate  
7 reached its maximum and then reduced after the CO<sub>2</sub> migrated around the fault tips. After this  
8 point, continued upward migration reduced the amount of CO<sub>2</sub> trapped below the fault,  
9 consequently decreasing the leakage rates (Figure 7d). This case demonstrates the tool's  
10 capability to capture several key aspects of fault-reservoir interaction. First, CO<sub>2</sub> accumulation  
11 at the fault barrier and subsequent lateral migration around fault tips reflects realistic plume  
12 behaviour in faulted systems. Second, the temporal evolution of leakage rates, increasing as  
13 CO<sub>2</sub> accumulates, then decreasing as the plume migrates past the fault, illustrates dynamic  
14 coupling between reservoir flow and fault leakage.

15  
16 Table 3 – Summary of model parameters used for the sloping reservoir simulation case  
17 described in section 3.3.

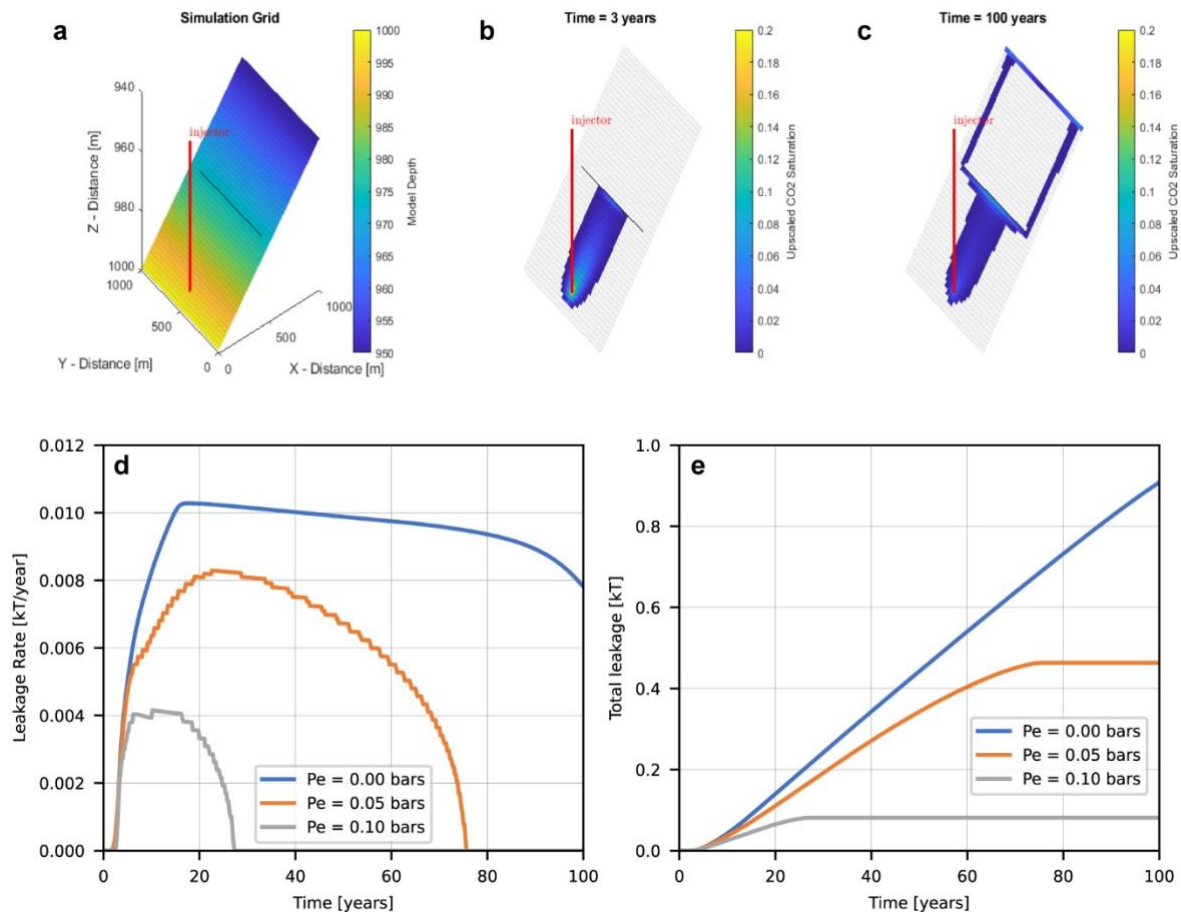
<b>Property</b>	<b>Value</b>
<b>Reservoir description</b>	
Number of cells (NX*NY)	50 x 50
Cell dimensions (DX*DY) (m)	20 x 20
Reservoir height (H) (m)	10
Reservoir slope (degrees)	2.86
Average reservoir depth (m)	975
Porosity	0.3
Permeability (mD)	100
Rock compressibility (Pa <sup>-1</sup> )	4.35 x 10 <sup>-10</sup>
<b>Fluid properties (at 2000m depth)</b>	
Brine viscosity (Pa.s)	3.13 x 10 <sup>-4</sup>
Gas viscosity (Pa.s)	3.21 x 10 <sup>-5</sup>
Brine density (kgm <sup>-3</sup> )	1001
Gas density (kgm <sup>-3</sup> )	389.7
<b>Fault damage zone properties</b>	
Fault damage zone permeability (mD)	1 x 10 <sup>-3</sup>
Fault damage zone width (m)	5
Fault damage zone length (m)	100

<b>Rock-Fluid properties</b>	
Residual gas saturation	0.2
Irreducible brine saturation	0.27

1

2           The introduction of a capillary entry pressure constraint for fault leakage reveals  
3 interesting leakage dynamics. Figure 7d depicts the leakage rates, while Figure 7e shows the  
4 cumulative leakage after 100 years for varying fault capillary entry pressures ranging from 0 to  
5 0.1 bar. Both the maximum fault leakage rate and cumulative leakage decrease with the increase  
6 in fault capillary entry pressure. The scenario with zero fault capillary entry pressure represents  
7 unconstrained leakage along the fault, allowing for continuous CO<sub>2</sub> leakage. In contrast, higher  
8 capillary entry pressures act as a barrier, limiting the extent of CO<sub>2</sub> migration and leakage  
9 through the fault zone. An important observation pertains to the leakage rate reaching zero. This  
10 occurs when the trapped CO<sub>2</sub> plume is unable to overcome the capillary entry pressure barrier,  
11 effectively stopping further leakage along the fault. The time at which leakage ceases decreases  
12 with the increase in fault capillary entry pressure, highlighting its potential for mitigating  
13 leakage.

14



1  
 2 Figure 7 – Simulation of CO<sub>2</sub> plume migration in a sloping reservoir (note vertical  
 3 exaggeration) and leakage along a fault showing the inclined 3D-view of the reservoir and the  
 4 location of the fault (a), the CO<sub>2</sub> plume saturation distribution at the end of the injection period  
 5 (b) the CO<sub>2</sub> plume saturation distribution after 100 years of migration (c), the CO<sub>2</sub> leakage rates  
 6 along the fault for different fault capillary entry pressures (d) and the cumulative CO<sub>2</sub> leakage  
 7 after 100 years for different fault capillary entry pressures (e).  
 8

### 9 3.4 Case 4 - Field-scale fault leakage quantification

10 The J area, a conceptual CO<sub>2</sub> storage site within the Malay Basin offshore Peninsular  
 11 Malaysia, is used to illustrate the fault leakage function coupled with VE models for field-scale  
 12 fault leakage quantification. The Malay Basin is approximately 500 km long, 200 km wide, and  
 13 12 km deep, situated in coastal waters less than 100 km from the east coast of Peninsular  
 14 Malaysia (de Jonge-Anderson et al., 2024b). It is a mature hydrocarbon basin with over 181  
 15 discoveries and over 14.8 billion barrels of oil equivalent in recoverable resources discovered  
 16 since 1981 (Madon, 2021). Recently, it has been considered an important area for CCS (Abd  
 17 Rahman et al., 2022; Hasbollah et al., 2020) due to its numerous mature fields that could be

1 repurposed, providing an abundance of data and production history. Saline aquifers offer great  
2 additional potential, however, limited data and understanding necessitate uncertainty  
3 assessment and screening analysis to determine storage traps.

4         The J area lies on the northern margin of the basin, 50 km from the nearest hydrocarbon  
5 field with the target reservoir situated at 1984 m depth below the seafloor. The main storage  
6 interval consists of a thick and heterogeneous sequence of lower to middle Miocene sandstones,  
7 mudstones, and coals, with the sandstones representing the target reservoir. The 3D reservoir  
8 grid, depths, petrophysical and reservoir properties are obtained from de Jonge-Anderson et al.  
9 (2024a, 2024b). These studies focused on storage capacity assessment without considering  
10 faults or leakage. Here we build on these studies and their well-characterized field-scale grid to  
11 demonstrate the applicability of the fault leakage function developed in this study. The relevant  
12 reservoir properties are summarized in Table 4. Previous storage capacity assessment for this  
13 site have identified the best injection location at the coordinate pair (413100 m, 718500 m)  
14 (UTM 48 N – reference coordinate system) for an injection rate of 1 Mt per year over 30 years  
15 followed by 970 years of migration (de Jonge-Anderson et al., 2024b). The top of the reservoir  
16 lies at depths between 1500 m and 2500 m below a seafloor depth of 70 m. The reservoir  
17 pressure is assumed hydrostatic with a temperature profile following a geothermal gradient of  
18 50°C/km and a seafloor temperature of 24°C (Madon & Jong, 2021).

19         The conceptual model comprising the storage reservoir connected to a secondary aquifer  
20 by a fault is shown in Figure 8. A 26 km-long fault is introduced into this grid as shown in  
21 Figure 9a and the fault properties are provided in Table 4. The fault introduced here is synthetic  
22 and designed specifically to evaluate the leakage modelling capabilities of the proposed  
23 methodology. Information was not available on actual fault properties in the J area, and  
24 characterization of real faults would be required for site-specific risk assessment. For the  
25 purposes of demonstrating our tool's field-scale applicability, the synthetic fault serves to

1 illustrate how the method can be applied to realistic reservoir geometries and evaluate  
 2 sensitivity to uncertain fault parameters. The synthetic fault is positioned to intersect the  
 3 reservoir and extend vertically into the caprock and hydraulically connect the storage reservoir  
 4 to a secondary aquifer. The grid blocks surrounding the fault are adjusted: 1) assign zero  
 5 transmissibility across the fault within the storage reservoir, representing an impermeable fault  
 6 core, and 2) insert the fault leakage function to mimic along fault leakage to secondary aquifer,  
 7 utilizing the properties listed in Table 4. Leakage is measured at the top of the fault (fault-  
 8 secondary aquifer interface), capturing the rate of CO<sub>2</sub> exiting the reservoir along the fault. The  
 9 injection well is located 12 km away from the fault. The model boundaries are treated as open,  
 10 with the pressure maintained at hydrostatic conditions. The goal of this case study is to  
 11 understand the impact of fault leakage on the injection rate and storage capacity within the J  
 12 area.

13



14

15

16 Figure 8 – The conceptual model of storage reservoir connected to a secondary aquifer by a  
 17 leaky fault is shown in cross-section view (a) and the storage reservoir is shown in plan view  
 18 (b).

19

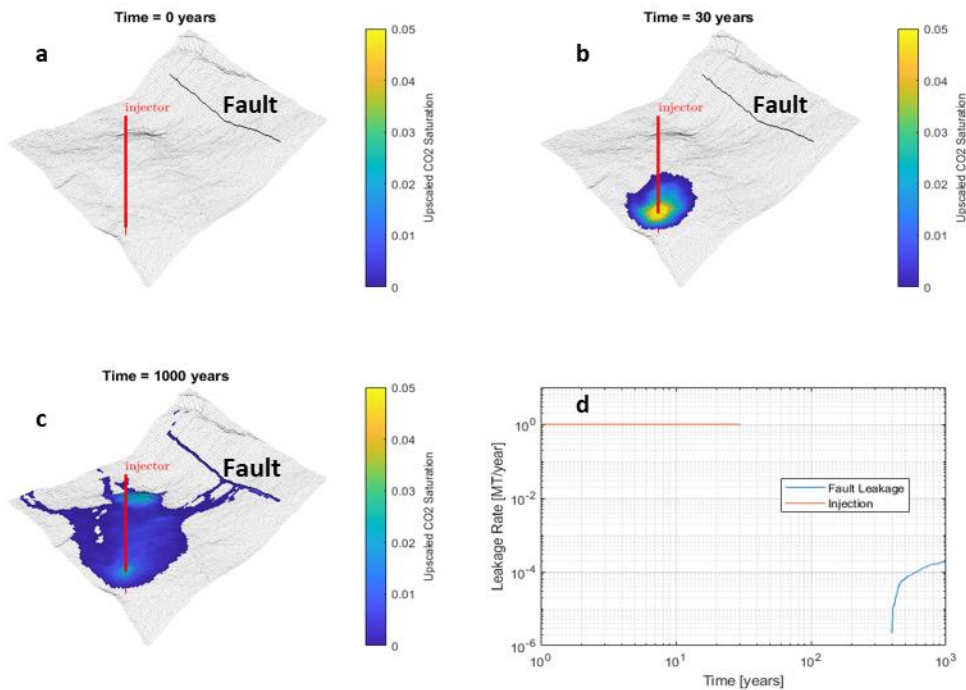
20 Table 4 – Summary of model parameters used for field-scale fault leakage quantification  
 21 simulation case described in section 3.4 (Adapted from (de Jonge-Anderson et al., 2024b))

Property	Value
<b>Reservoir description</b>	
Number of cells (NX*NY*NZ)	100 x 110 x 5
Cell dimensions (DX*DY) (m)	200 x 200
Area (km <sup>2</sup> )	440 (22 x 20)
Average top reservoir depth (m)	1984
Porosity	0.05 – 0.25 (arithmetic mean = 0.145)

Permeability (mD)	1.2 –241 (arithmetic mean = 39.4)
Rock compressibility (Pa <sup>-1</sup> )	4.35 x 10 <sup>-10</sup>
Seafloor temperature (°C)	24
Temperature gradient (°Ckm <sup>-1</sup> )	50
Seafloor Depth (m)	70
<b>Fluid properties (at 2000m depth)</b>	
Brine viscosity (Pa.s)	3.13 x 10 <sup>-4</sup>
Gas viscosity (Pa.s)	3.21 x 10 <sup>-5</sup>
Brine density (kgm <sup>-3</sup> )	1001
Gas density (kgm <sup>-3</sup> )	389.7
<b>Fault damage zone properties</b>	
Fault damage zone permeability (mD)	1 x 10 <sup>-3</sup>
Fault damage zone width (m)	5
Fault damage zone length (m)	500
<b>Rock-Fluid properties (Brooks-Corey Model)</b>	
Residual gas saturation	0.2
Irreducible brine saturation	0.27
Gas end-point relative permeability	1
Brine end-point relative permeability	1
Gas relative permeability exponent	1
Brine relative permeability exponent	1

1

2

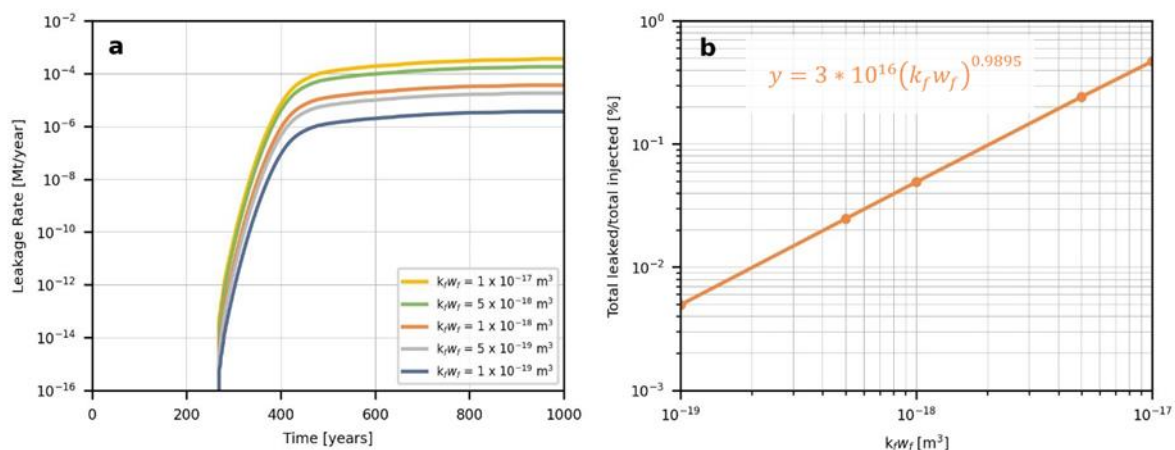


3

4 Figure 9 – Simulation of CO<sub>2</sub> plume migration and leakage along a leaky fault. Inclined 3D  
 5 view of the reservoir showing the location of the fault (a), CO<sub>2</sub> plume saturation distribution at

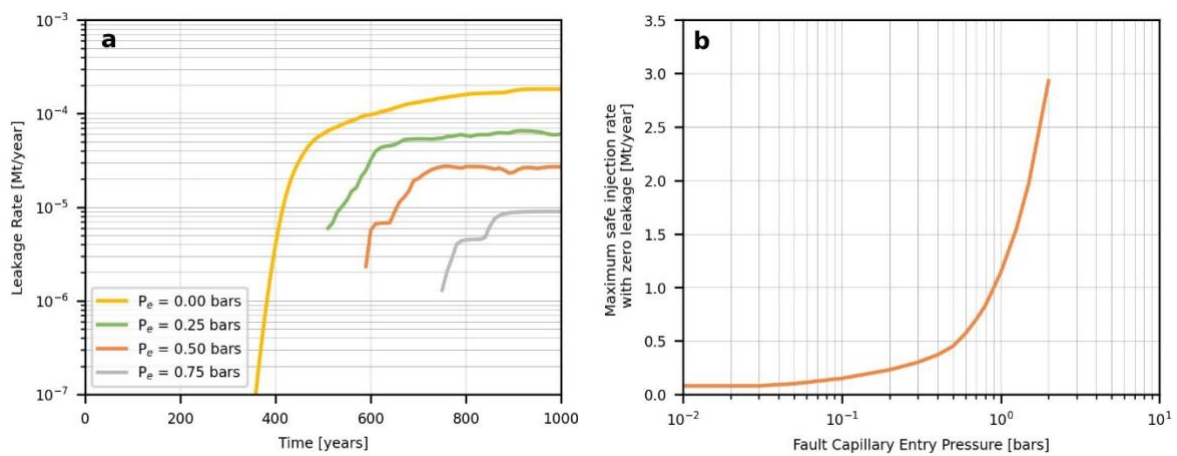
1 the end of the injection period (b), CO<sub>2</sub> plume saturation distribution after 1000 years of  
2 migration (c) and temporal evolution of the CO<sub>2</sub> leakage rate along the fault (d).

3  
4 A numerical simulation is performed to assess the impact of a fault on the migration and  
5 leakage of a CO<sub>2</sub> injected into the reservoir (Figure 9a). The evolution of the CO<sub>2</sub> plume is  
6 depicted at the end of the injection period (Figure 9b) and after 1000 years of the migration  
7 phase (Figure 9c). The simulation results show the CO<sub>2</sub> plume moving up-dip and accumulating  
8 within an anticline structure. Considerable amounts of CO<sub>2</sub> accumulate at the base of the fault,  
9 with the impermeable fault core preventing further migration across the fault. The CO<sub>2</sub> plume  
10 reaches the fault after approximately 400 years and immediately begins leaking through the  
11 fault (Figure 9d). The leakage rate increases as more of the migrating CO<sub>2</sub> became trapped at  
12 the faulted block representing the hanging wall. By the end of the 1,000-year simulation period,  
13 a total of 30 Mt of CO<sub>2</sub> has been injected, of which 0.085 Mt (0.28%) has leaked along the fault.  
14 These results highlight the impact that the presence of a fault can have on the migration and  
15 containment of a CO<sub>2</sub> plume in a storage setting and the ability to address this impact quickly  
16 as each simulation takes under 30 seconds on Apple MacBook Pro with the Apple M1 chip.



18  
19 Figure 10 – Impact of fault properties on CO<sub>2</sub> leakage showing the relationship between fault  
20 permeability, damage zone thickness, and the magnitude of CO<sub>2</sub> leakage (a) and the decrease  
21 in total CO<sub>2</sub> leakage over time with decreasing value for the product of fault permeability and  
22 damage zone thickness  $k_f w_f$  (b).  
23

1 The fault permeability and the thickness of the damage zone play a crucial role in  
 2 determining the magnitude of CO<sub>2</sub> leakage, as shown in Figure 8. While these parameters do  
 3 not affect the onset of leakage (Figure 10a). The total amount of leakage decreases, following  
 4 a power-law trend with an exponent of 0.9895 as the product of fault permeability and damage  
 5 zone thickness  $k_f w_f$  decreases (Figure 10b). While Equation 16 predicted an exponent of 1, the  
 6 observed deviation suggests that variations in pressure buildup induced by fault permeability  
 7 also influence leakage rates. These effects are captured within the presented function. The fault  
 8 permeability is strongly dependent on the thickness of the damage zone, as well as the inter-  
 9 connectedness and density of the fracture networks within the damage zone, and studies have  
 10 demonstrated that these fault zone parameters are influenced by the pressure within the  
 11 reservoir-caprock-fault system (Rutqvist 2012; Vilarrasa et al., 2017).  
 12



13 Figure 11 – Impact of fault capillary entry pressure on CO<sub>2</sub> leakage showing the leakage profile  
 14 for different fault capillary entry pressures where higher entry pressures act as a barrier,  
 15 delaying and reducing the CO<sub>2</sub> leakage and no leakage occurs for a scenario of 1 bar (a).  
 16 Maximum injection rate with zero leakage for a range of fault capillary entry pressures where  
 17 increasing the entry pressure allows for higher injection rates without CO<sub>2</sub> leakage (b).  
 18  
 19

20 The fault damage zone capillary entry pressure represents the minimum differential  
 21 pressure required for CO<sub>2</sub> to overcome and enter the fault damage zone, controlled by the  
 22 effective aperture of the largest pore throats or fracture openings (Monzocchi et al., 2010;

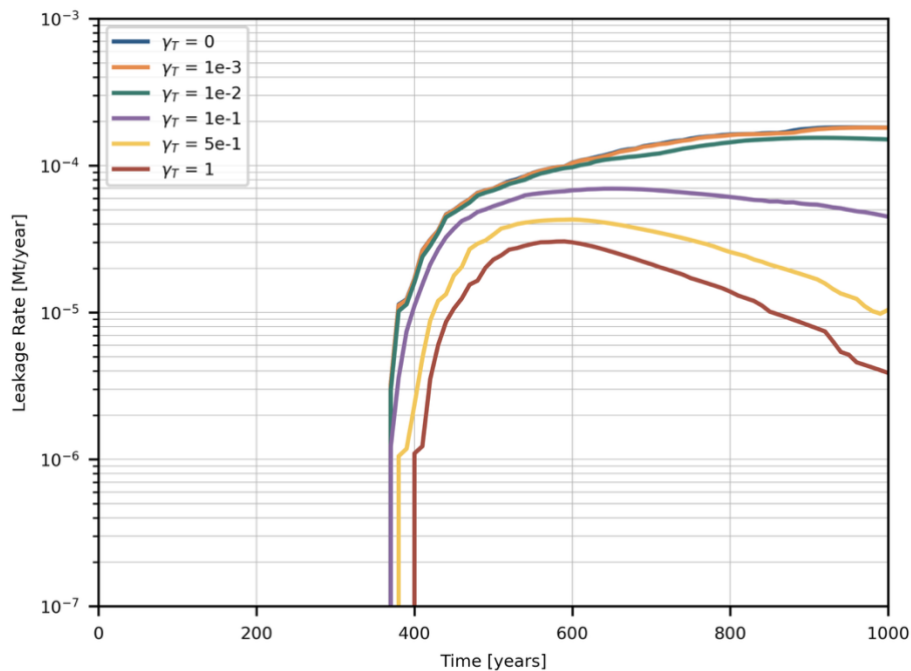
1 Espinoza et al., 2017; Zheng and Espinoza, 2022). The physics of leakage governed by capillary  
2 entry pressure has been demonstrated through theoretical and experimental studies showing that  
3 flow occurs where fluid pressure exceeds this threshold (Sayag and Neufeld, 2016).  
4 Importantly, as shown in Equation 15, the driving potential for fault leakage depends on the  
5 combined effects of buoyancy from CO<sub>2</sub> accumulation, injection-induced reservoir  
6 overpressure, and the resisting capillary entry pressure. This coupling means that fault leakage  
7 behaviour depends on both geological properties (entry pressure, permeability), fluid properties  
8 (buoyancy) and operational decisions (injection rate and pressure, total injected volume, well  
9 placement). The ability to rapidly evaluate these trade-offs between geological uncertainty and  
10 operational constraints is essential during site screening when multiple candidates and injection  
11 strategies must be assessed.

12 We demonstrate this capability by varying fault capillary entry pressures (Figure 11) in  
13 the preceding simulation for the J area. As the entry pressure increases from 0 to 0.75 bar,  
14 leakage onset is progressively delayed, and maximum leakage rates decrease due to the reduced  
15 driving potential. For this specific injection scenario (1 Mt/year for 30 years) and reservoir  
16 configuration, an entry pressure of 1.0 bar prevents any leakage over the 1000-year simulation  
17 period. Figure 11b shows that higher entry pressures permit higher injection rates before  
18 leakage occurs. The observation that a 1 bar entry pressure prevents leakage in this scenario  
19 reflects the specific pressure evolution and CO<sub>2</sub> accumulation pattern resulting from the  
20 reservoir-injection configuration. With injection 12 km from the fault, pressure diffusion over  
21 this distance limits overpressure at the fault location, while the buoyancy-driven accumulation  
22 produces a CO<sub>2</sub> column insufficient to generate the equivalent 17-meter height needed to  
23 overcome the 1 bar threshold. The combined driving potential (buoyancy plus overpressure)  
24 never exceeds the capillary barrier. A different configuration, for instance, injection closer to  
25 the fault or a structural setting promoting greater CO<sub>2</sub> accumulation at the fault base could

1 generate higher driving potentials, making the same 1 bar entry pressure insufficient to prevent  
2 leakage. This sensitivity highlights that fault sealing capacity cannot be assessed from entry  
3 pressure alone; it depends critically on the interplay between reservoir-scale pressure  
4 propagation, CO<sub>2</sub> migration patterns, and fault properties.

5 Our earlier analysis assumed zero across-fault flow (transmissibility multiplier,  $\gamma_T =$   
6 0), representing a worst-case scenario where the low-permeability fault core acts as a complete  
7 barrier within the reservoir. In reservoir simulation, transmissibility multipliers quantify the  
8 hydraulic conductivity across faults, scaling the flow between adjacent grid cells from 0  
9 (complete sealing) to 1 (no flow impedance). These multipliers depend on fault zone properties  
10 including fault core thickness and permeability relative to the reservoir rock (Manzocchi et al.,  
11 1999). To assess the sensitivity of leakage predictions to this assumption, we conducted  
12 simulations with  $\gamma_T$  values ranging from 0 to 1.0, maintaining zero fault capillary entry pressure  
13 and all other parameters from Table 4. This analysis considers only across fault transmissibility;  
14 capillary barriers within the fault core are not included.

15



16

1 Figure 12 – Sensitivity of leakage rates to transmissibility multiplier ( $\gamma_T$ ). Six cases are shown  
2 ranging from completely sealed ( $\gamma_T = 0$ ) to fully permeable ( $\gamma_T = 1$ ) fault cores. Total  
3 cumulative leakage over 1000 years is shown in the legend.  
4

5 Figure 12 shows that cumulative leakage decreases substantially as across-fault flow  
6 increases. The zero-flow assumption ( $\gamma_T = 0$ ) yields maximum leakage with a case having  
7 essentially impermeable fault ( $\gamma_T = 10^{-3}$ ) producing nearly identical results. This verifies our  
8 conservative assumption that highly sealing faults behave similarly to completely sealed faults.  
9 However, as transmissibility multiplier increases beyond  $10^{-3}$ , leakage rates decline  
10 progressively, with  $\gamma_T = 0.1$  reducing total leakage by approximately 55% and  $\gamma_T = 1$  (fully  
11 permeable fault core) reducing it by 87% relative to the sealed case. When the fault core allows  
12 flow, migrating CO<sub>2</sub> can pass through the fault within the reservoir. This reduces the plume  
13 height of CO<sub>2</sub> along the fault base, decreasing the driving potential for vertical leakage. These  
14 results demonstrate that the zero across-fault flow assumption provides an upper bound on  
15 leakage estimates, appropriate for conservative early-stage screening when fault core properties  
16 are uncertain.

## 17 4 Discussion

18 One of the key strengths of the proposed approach is its computational efficiency. By  
19 employing the VE approximation instead of 3D grids and detailed multiphase flow simulations,  
20 the model significantly reduces processing time and resources (Nordbotten & Celia, 2011;  
21 Nilsen et al., 2016). For example, in the Malay Basin case study (Section 3.4), it produced  
22 predictive results for a 440 km<sup>2</sup> area with a leaky fault in under 30 seconds. This speed is  
23 particularly valuable for early-stage CCS project development, where multiple candidate sites  
24 must be rapidly screened (Pawar et al., 2015). In addition, the simplicity of the analytical fault  
25 leakage function enables straightforward integration into established VE simulation workflows,  
26 promoting wider adoption, especially for projects limited by sparse data or computational  
27 resources (Andersen, 2017).

1           The four simulation cases highlight the model's versatility in assessing along-fault  
2 leakage under varying conditions. Case 1 demonstrated strong agreement between VE-fault  
3 leakage function results and 2D numerical simulations with explicitly gridded faults,  
4 confirming the analytical fault leakage function's accuracy. Case 2 revealed the model's  
5 robustness under varying grid resolutions and time step sizes; although coarser grids and larger  
6 time steps initially overestimated leakage rates, the results converged at steady state, ensuring  
7 stability across different computational setups. In Case 3, introducing fault capillary entry  
8 pressure in a sloping reservoir scenario revealed its critical influence on leakage control: higher  
9 entry pressures delayed leakage onset and reduced cumulative leakage, underscoring the  
10 importance of this parameter in CCS design. Finally, Case 4 applied the model to the field-scale  
11 Malay Basin, showing leakage sensitivity for wide range of certain parameters and  
12 demonstrating its practical applicability in realistic geological settings. Our assumption of zero  
13 across-fault flow within the reservoir represents a conservative worst-case scenario. In reality,  
14 fault cores often have finite permeability allowing some across-fault flow (Manzocchi et al.,  
15 2010; Yielding et al., 2010; Pei et al., 2015; Ketterman et al., 2020), which would reduce CO<sub>2</sub>  
16 accumulation at the fault base and decrease vertical leakage. Section 3.4 demonstrates how  
17 incorporating across-fault flow through transmissibility multipliers affects leakage predictions.

18           Collectively, these cases deepen our understanding of how fault properties impact  
19 leakage behaviour. Increased fault permeability, particularly under pressure-driven conditions,  
20 can substantially elevate leakage rates, emphasizing the need for detailed permeability  
21 characterization during site selection (Bjørnarå et al., 2023; Salo-Salgado et al., 2023; Rizzo et  
22 al., 2024). The capillary entry pressure analysis illustrated the interaction between operational  
23 conditions (injection rate and pressure, pressure buildup) and geological properties (capillary  
24 entry pressure) in controlling leakage onset and magnitude. Higher capillary entry pressure  
25 delayed leakage onset and reduced cumulative leakage, demonstrating how this parameter

1 constrains the driving potential for fault leakage (Equation 15). Beyond these individual  
2 insights, the model's ability to rapidly evaluate fault leakage risks enables strategic decision-  
3 making in geologically complex settings. By identifying sites with lower containment risks  
4 early on, the model helps allocate computational resources more efficiently. On the other hand,  
5 if gigatonne-scale storage is to be achieved in the coming decades (Krevor et al., 2023), it is  
6 imperative to move beyond the simpler 'Class A' storage sites (Ringrose & Meckel, 2019).  
7 These could include sites with a degree of fault-related leakage risk and this model's scalability,  
8 and speed could prove crucial to rapidly evaluating and de-risking such areas.

9         An inherent challenge in fault modelling is the uncertainty associated with fault property  
10 data. Although it is helpful that the proposed model captured the sensitivity of fault permeability  
11 and fault capillary entry pressure on total leakage, obtaining more detailed data on fault  
12 geometry, stress regimes, and fracture networks could improve the accuracy of leakage  
13 predictions (Snippe et al., 2022; Rizzo et al., 2024). The assumption of constant fault  
14 permeability and capillary entry pressure may not adequately capture the heterogeneity present  
15 in real-world faults. Future studies should explore the impact of spatial variability in fault  
16 properties using stochastic modelling techniques (Berge et al., 2022; Bjørnarå et al., 2023; Salo-  
17 Salgado et al., 2023). The model assumes pre-existing fault permeability and does not account  
18 for stress-induced permeability changes, fault reactivation, or pressure-stress coupling. These  
19 geomechanical processes can significantly alter leakage behaviour, particularly over decadal to  
20 centennial timescales, and have been demonstrated to control leakage onset, duration, and  
21 magnitude (Rutqvist, 2012; Rinaldi et al., 2014; Jha and Juanes, 2014; Vilarrasa et al., 2017;  
22 Chang and Segall, 2016; Meguerdijian and Jha, 2021; Zhao and Jha, 2019; Castelletto et al.,  
23 2013; Chen et al., 2024). Fault reactivation and fracture opening can increase damage zone  
24 permeability by a few orders of magnitude, though the magnitude of change varies significantly  
25 with fault architecture and stress conditions (Simpson et al., 2001; Mitchell & Faulkner, 2012;

1 Petrie et al., 2014; Aben et al., 2020; Rizzo et al., 2024). In particular, if a fault is critically  
2 stressed, injection pressures sufficient for storage operations could induce reactivation and  
3 elevate permeability beyond the range considered during screening, potentially causing the  
4 model to underestimate leakage risk and misclassify a site as suitable for storage. Moreover,  
5 positive feedback mechanisms, such as fault slip triggering further fracture opening which  
6 accelerates permeability increase are not represented here. Nevertheless, the sensitivity  
7 analyses presented in Case 4 evaluate leakage across fault permeability ranges that encompass  
8 values produced by activation, allowing potential risks to be bounded without explicitly  
9 modelling the underlying mechanisms. The computational efficiency of the proposed approach  
10 makes such wide-range parameter exploration tractable at the screening stage. In fields  
11 containing multiple faults, this capability allows the identification of faults that pose the greatest  
12 leakage risk, thereby focusing data acquisition efforts and subsequent coupled geomechanical  
13 simulations. While the model has been verified against synthetic scenarios and benchmark  
14 simulations, further validation using real-world datasets would strengthen its applicability and  
15 reliability (Michie et al., 2021; Choi et al., 2023).

## 16 5 Conclusions

17 This work presents a fast and computationally efficient tool for simulating fault leakage  
18 under uncertainty for realistic, field-scale CO<sub>2</sub> storage applications. Faults are inherently  
19 complex, typically characterized by a fault core and a surrounding fractured damage zone, both  
20 of which significantly influence fault leakage behaviour at the field scale. Explicitly  
21 representing these fault complexities along with the multi-layered systems is a computationally  
22 intensive method for resolving fault leakage-related uncertainty, especially during the early  
23 stages of storage site screening when data availability is limited. The primary contribution of  
24 this work addresses this challenge by proposing an approach that integrates an upscaled fault  
25 leakage function, specifically tailored to the unique characteristics of the fault core, damage

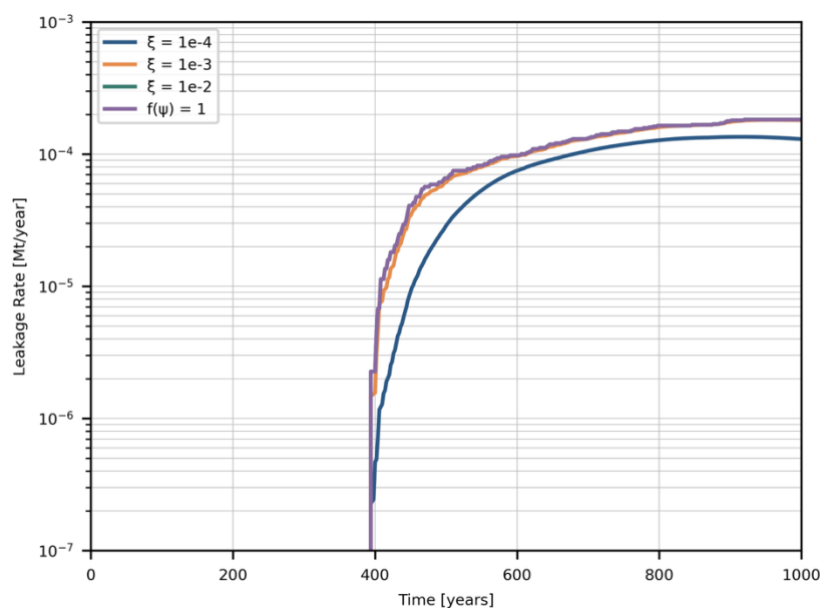
1 zone, and flow properties, into a VE reservoir modelling framework. The proposed tool is a  
2 cost-effective method for early-stage screening of fault leakage risk during CO<sub>2</sub> storage site  
3 selection. By enabling rapid evaluation of multiple sites and uncertainty scenarios, it allows  
4 identification of potential suitable candidates warranting detailed investigation. Sites identified  
5 through this screening process should subsequently undergo rigorous coupled thermal-  
6 geomechanical-dynamic modelling for detailed characterization, with the screening results  
7 directly informing which faults require detailed geomechanical characterization and which  
8 parameters dominate leakage risk. This two-stage workflow allows strategic allocation of  
9 computational and data acquisition resources to sites with greatest storage potential. The tool's  
10 computational efficiency, demonstrated by 30-second runtimes for the Malay Basin case study,  
11 enables the extensive uncertainty quantification necessary during early project stages when  
12 subsurface data is limited. Such fast screening of potential storage sites is key to enabling the  
13 scale-up of CO<sub>2</sub> storage and achieving the gigaton-scale deployment needed to reduce global  
14 CO<sub>2</sub> emissions.

15         The findings from the simulation cases provide valuable insights into the roles of fault  
16 permeability and capillary entry pressure in controlling CO<sub>2</sub> leakage rates. The results highlight  
17 the importance of accurately characterizing these fault properties and incorporating capillary  
18 entry pressure constraints into CCS site assessments. The ability of the proposed model to  
19 handle a range of scenarios, from synthetic benchmarks to field-scale applications,  
20 demonstrates its versatility and practical relevance to CO<sub>2</sub> storage characterization studies. The  
21 current assumptions of steady-state leakage and constant fault properties limit the ability to  
22 capture dynamic behaviours such as fault reactivation or pressure changes over time. Future  
23 studies should address these limitations by incorporating geomechanical processes and  
24 stochastic variability in fault properties. Additionally, testing the model against diverse field  
25 datasets will enhance confidence in its broader applicability and reliability.

## 1 Appendix A: Sensitivity to smoothing parameter

2 The smoothing parameter  $\xi$  in the fault leakage function (Section 2.3, Equation 16)  
3 regulates the transition when the driving potential  $\psi$  approaches the capillary entry pressure  
4 threshold and the initial occurrence of a non-zero fault leakage term. To assess whether  
5 simulation results are sensitive to this parameter, we conducted an analysis using the simulation  
6 setup from case 4 (section 3.4) with zero capillary entry pressure and parameters specified in  
7 Table 4. Figure A1 shows the temporal evolution of fault leakage rates for three different  
8 smoothing parameter values ( $\xi = 10^{-4}$ ,  $10^{-3}$ , and  $10^{-2}$  Pa $^{-1}$ ) alongside a case with no smoothing  
9 ( $f(\psi) = 1$ , i.e.  $\xi \rightarrow \infty$ ). All four curves are nearly identical, except for  $\xi = 10^{-4}$  Pa $^{-1}$  where it  
10 underpredicted leakage, demonstrating that the smoothing parameter has minimal impact on  
11 leakage magnitudes for  $\xi > 10^{-3}$  Pa $^{-1}$ . This is because the smoothing function primarily affects  
12 behaviour when  $\psi$  is within a few pascals of the threshold. For typical CO $_2$  storage conditions,  
13 where driving potentials significantly exceed this narrow transition zone, the smoothing has  
14 negligible impact on predicted leakage rates. The value  $\xi = 10^{-3}$  Pa $^{-1}$  used throughout this study  
15 provides numerical stability without meaningfully altering results.

16



17

1 Figure A1 – Sensitivity of fault leakage rates to the smoothing parameter  $\xi$  for the Malay Basin  
2 case with zero fault capillary entry pressure. Four cases are shown:  $\xi = 10^{-4} \text{ Pa}^{-1}$  (blue),  $\xi = 10^{-3}$   
3  $\text{ Pa}^{-1}$  (orange),  $\xi = 10^{-2} \text{ Pa}^{-1}$  (green), and no smoothing with  $f(\psi) = 1$  (light blue).  
4

## 5 Data Availability Statement

6 Simulations were conducted using the co2-lab module of the open-source MATLAB®  
7 Reservoir Simulation Toolbox, MRST, available at <https://www.sintef.no/projectweb/mrst/>.  
8 The fault leakage function module is on GitHub (<https://github.com/Poriyalar/faultve>) and  
9 available at zenodo (Ramachandran., 2025).

## 10 Conflict of Interest Statement

11 The authors have no conflicts of interest to disclose.

## 12 Acknowledgements

13 The funding and data underpinning this work was provided by PETRONAS via the  
14 PETRONAS Centre of Excellence in Subsurface Engineering and Energy Transition  
15 (PACESET), based at Heriot-Watt University. Sebastian Geiger thanks Energi Simulation for  
16 supporting his Chair in Sustainable Geoenergy. Florian Doster acknowledge valuable  
17 discussions with Michael A. Celia, Jan M. Nordbotten and Mary Kang while formulating the  
18 research topic.

## 19 References

- Abd Rahman, I. Z., Abang Hasbollah, D. Z., Mohd Yunus, N. Z., Kasiman, E. H., & Mazlan, A. N. (2022). Carbon dioxide storage potential in malaysian sandstone aquifer: An overview. *IOP Conference Series: Earth and Environmental Science*, 971(1), 012022. <https://doi.org/10.1088/1755-1315/971/1/012022>
- Aben, F. M., Doan, M., & Mitchell, T. M. (2020). Variation of hydraulic properties due to dynamic fracture damage: Implications for fault zones. *Journal of Geophysical Research: Solid Earth*, 125(4), e2019JB018919. <https://doi.org/10.1029/2019JB018919>
- Andersen, O. (2017). *Simplified models for numerical simulation of geological CO2 storage* [Doctoral thesis, The University of Bergen]. <https://bora.uib.no/bora-xmlui/handle/1956/15477>

- Andersen, O. A., Nilsen, H. M., & Gasda, S. E. (2016, August 29). *Modelling geomechanical impact of co2 injection and migration using precomputed response functions*. ECMOR XV - 15th European Conference on the Mathematics of Oil Recovery, Amsterdam, Netherlands. <https://doi.org/10.3997/2214-4609.201601760>
- Andersen, O. A., Nilsen, H. M., & Gasda, S. E. (2017). Vertical equilibrium flow models with fully coupled geomechanics for co2 storage modeling, using precomputed mechanical response functions. *Energy Procedia*, 114, 3113–3131. <https://doi.org/10.1016/j.egypro.2017.03.1440>
- Andersen, O., Gasda, S. E., & Nilsen, H. M. (2015). Vertically averaged equations with variable density for co2 flow in porous media. *Transport in Porous Media*, 107(1), 95–127. <https://doi.org/10.1007/s11242-014-0427-z>
- Anderson, S. T. (2017). Risk, liability, and economic issues with long-term CO2 storage—A review. *Natural Resources Research*, 26(1), 89–112. <https://doi.org/10.1007/s11053-016-9303-6>
- Ashworth, P., Wade, S., Reiner, D., & Liang, X. (2015). Developments in public communications on CCS. *International Journal of Greenhouse Gas Control*, 40, 449–458. <https://doi.org/10.1016/j.ijggc.2015.06.002>
- Bachu, S. (2008). Legal and regulatory challenges in the implementation of CO2 geological storage: An Alberta and Canadian perspective☆. *International Journal of Greenhouse Gas Control*, 2(2), 259–273. <https://doi.org/10.1016/j.ijggc.2007.12.003>
- Ballas, G., Fossen, H., & Soliva, R. (2015). Factors controlling permeability of cataclastic deformation bands and faults in porous sandstone reservoirs. *Journal of Structural Geology*, 76, 1–21. <https://doi.org/10.1016/j.jsg.2015.03.013>
- Bandilla, K. W., Celia, M. A., & Leister, E. (2014). Impact of model complexity on co2 plume modeling at sleipner. *Energy Procedia*, 63, 3405–3415. <https://doi.org/10.1016/j.egypro.2014.11.369>
- Becker, B., Guo, B., Bandilla, K., Celia, M. A., Flemisch, B., & Helmig, R. (2017). A pseudo-vertical equilibrium model for slow gravity drainage dynamics. *Water Resources Research*, 53(12), 10491–10507. <https://doi.org/10.1002/2017WR021644>
- Becker, B., Guo, B., Bandilla, K., Celia, M. A., Flemisch, B., & Helmig, R. (2018). An adaptive multiphysics model coupling vertical equilibrium and full multidimensions for multiphase flow in porous media. *Water Resources Research*, 54(7), 4347–4360. <https://doi.org/10.1029/2017WR022303>
- Becker, B., Guo, B., Buntic, I., Flemisch, B., & Helmig, R. (2022). An adaptive hybrid vertical equilibrium/full-dimensional model for compositional multiphase flow. *Water Resources Research*, 58(1), e2021WR030990. <https://doi.org/10.1029/2021WR030990>
- Bense, V. F., & Person, M. A. (2006). Faults as conduit-barrier systems to fluid flow in siliciclastic sedimentary aquifers. *Water Resources Research*, 42(5), 2005WR004480. <https://doi.org/10.1029/2005WR004480>
- Berge, R. L., Gasda, S. E., Keilegavlen, E., & Sandve, T. H. (2022). Impact of deformation bands on fault-related fluid flow in field-scale simulations. *International Journal of Greenhouse Gas Control*, 119, 103729. <https://doi.org/10.1016/j.ijggc.2022.103729>
- Bielicki, J. M., Pollak, M. F., Fitts, J. P., Peters, C. A., & Wilson, E. J. (2014). Causes and financial consequences of geologic CO2 storage reservoir leakage and interference with other subsurface resources. *International Journal of Greenhouse Gas Control*, 20, 272–284. <https://doi.org/10.1016/j.ijggc.2013.10.024>
- Bjørnarå, T. I., Nordbotten, J. M., & Park, J. (2016). Vertically integrated models for coupled two-phase flow and geomechanics in porous media. *Water Resources Research*, 52(2), 1398–1417. <https://doi.org/10.1002/2015WR017290>

- Bjørnarå, T. I., Skurtveit, E., Michie, E. A. H., & Smith, S. A. (2023). Characterizing along- and across-fault fluid-flow properties for assessing flow rates and overburden fluid migration along faults: A case study from the North Sea. *Petroleum Geoscience*, 29(3), petgeo2023-033. <https://doi.org/10.1144/petgeo2023-033>
- Caine, J. S., Evans, J. P., & Forster, C. B. (1996). Fault zone architecture and permeability structure. *Geology*, 24(11), 1025. [https://doi.org/10.1130/0091-7613\(1996\)024<1025:FZAAPS>2.3.CO;2](https://doi.org/10.1130/0091-7613(1996)024<1025:FZAAPS>2.3.CO;2)
- Castelletto, N., Gambolati, G., & Teatini, P. (2013). Geological CO<sub>2</sub> sequestration in multi-compartment reservoirs: Geomechanical challenges. *Journal of Geophysical Research: Solid Earth*, 118(5), 2417–2428. <https://doi.org/10.1002/jgrb.50180>
- Celia, M. A., Bachu, S., Nordbotten, J. M., & Bandilla, K. W. (2015). Status of CO<sub>2</sub> storage in deep saline aquifers with emphasis on modelling approaches and practical simulations. *Water Resources Research*, 51(9), 6846–6892. <https://doi.org/10.1002/2015WR017609>
- Chang, K. W., & Segall, P. (2016). Injection-induced seismicity on basement faults including poroelastic stressing. *Journal of Geophysical Research: Solid Earth*, 121(4), 2708–2726. <https://doi.org/10.1002/2015JB012561>
- Chen, L., Elsworth, D., Chen, J., & Gan, Q. (2024). Evaluation of CO<sub>2</sub> leakage potential through fault instability in CO<sub>2</sub> geological sequestration by coupled THMC modelling. *Gas Science and Engineering*, 132, 205486. <https://doi.org/10.1016/j.jgsce.2024.205486>
- Childs, C., Manzocchi, T., Walsh, J. J., Bonson, C. G., Nicol, A., & Schöpfer, M. P. J. (2009). A geometric model of fault zone and fault rock thickness variations. *Journal of Structural Geology*, 31(2), 117–127. <https://doi.org/10.1016/j.jsg.2008.08.009>
- Choi, J. C., Skurtveit, E., Huynh, K. D. V., & Grande, L. (2023). Uncertainty of stress path in fault stability assessment during CO<sub>2</sub> injection: Comparing smeaeheia 3D geomechanics model with analytical approaches. *International Journal of Greenhouse Gas Control*, 125, 103881. <https://doi.org/10.1016/j.ijggc.2023.103881>
- Climate Change Committee (2021). Independent assessment: The uk's net zero strategy. (n.d.). Climate Change Committee. Retrieved March 12, 2024, from <https://www.theccc.org.uk/publication/independent-assessment-the-uks-net-zero-strategy/>
- de Jonge-Anderson, I., Ramachandran, H., Nicholson, U., Geiger, S., Widyanita, A., & Doster, F. (2024a). Determining CO<sub>2</sub> storage efficiency within a saline aquifer using reduced complexity models. *Advances in Geo-Energy Research*, 13(1), 22–31. <https://doi.org/10.46690/ager.2024.07.04>
- de Jonge-Anderson, I., Widyanita, A., Busch, A., Doster, F., & Nicholson, U. (2024b). New insights into the structural and stratigraphic evolution of the Malay Basin using 3D seismic data: Implications for regional carbon capture and storage potential. *Basin Research*, 36(4), e12885. <https://doi.org/10.1111/bre.12885>
- Department of Geology, Universiti Malaya, 50603 Kuala Lumpur, Malaysia, & Madon, M. (2021). Five decades of petroleum exploration and discovery in the malay basin (1968-2018) and remaining potential. *Bulletin Of The Geological Society Of Malaysia*, 72, 63–88. <https://doi.org/10.7186/bgs72202106>
- Derrell A. Smith (2). (1980). Sealing and nonsealing faults in louisiana gulf coast salt basin. *AAPG Bulletin*, 64. <https://doi.org/10.1306/2F918946-16CE-11D7-8645000102C1865D>
- Dewhurst, D. N., Delle Piane, C., Esteban, L., Sarout, J., Josh, M., Pervukhina, M., & Clennell, M. B. (2018). Microstructural, geomechanical, and petrophysical characterization of shale caprocks. In S. Vialle, J. Ajo-Franklin, & J. W. Carey

- (Eds.), *Geophysical Monograph Series* (1st ed., pp. 1–30). Wiley.  
<https://doi.org/10.1002/9781119118657.ch1>
- Dixon, T., McCoy, S. T., & Havercroft, I. (2015). Legal and regulatory developments on ccs. *International Journal of Greenhouse Gas Control*, *40*, 431–448.  
<https://doi.org/10.1016/j.ijggc.2015.05.024>
- Doster, F., Nordbotten, J. M., & Celia, M. A. (2012). Hysteretic upscaled constitutive relationships for vertically integrated porous media flow. *Computing and Visualization in Science*, *15*(4), 147–161. <https://doi.org/10.1007/s00791-013-0206-3>
- Doster, F., Nordbotten, J. M., & Celia, M. A. (2013). Impact of capillary hysteresis and trapping on vertically integrated models for CO<sub>2</sub> storage. *Advances in Water Resources*, *62*, 465–474. <https://doi.org/10.1016/j.advwatres.2013.09.005>
- Du Plessis, E., Nordbotten, J. M., Gasda, S. E., & Dahle, H. K. (2013). Influence of capillary pressure and trapping hysteresis on large-scale CO<sub>2</sub> migration. *Journal of Coupled Systems and Multiscale Dynamics*, *1*(4), 442–458.  
<https://doi.org/10.1166/jcsmd.2013.1030>
- Espinoza, D. N., & Santamarina, J. C. (2017). CO<sub>2</sub> breakthrough—Caprock sealing efficiency and integrity for carbon geological storage. *International Journal of Greenhouse Gas Control*, *66*, 218–229. <https://doi.org/10.1016/j.ijggc.2017.09.019>
- Fachri, M., Tveranger, J., Braathen, A., & Schueller, S. (2013). Sensitivity of fluid flow to deformation-band damage zone heterogeneities: A study using fault facies and truncated Gaussian simulation. *Journal of Structural Geology*, *52*, 60–79.  
<https://doi.org/10.1016/j.jsg.2013.04.005>
- Faulkner, D. R., Jackson, C. A. L., Lunn, R. J., Schlische, R. W., Shipton, Z. K., Wibberley, C. A. J., & Withjack, M. O. (2010). A review of recent developments concerning the structure, mechanics and fluid flow properties of fault zones. *Journal of Structural Geology*, *32*(11), 1557–1575. <https://doi.org/10.1016/j.jsg.2010.06.009>
- G. Yielding, B. Freeman, And D. T. Needham (1997). Quantitative fault seal prediction. *AAPG Bulletin*, *81* (1997). <https://doi.org/10.1306/522B498D-1727-11D7-8645000102C1865D>
- Gasda, S. E., Nordbotten, J. M., & Celia, M. A. (2011). Vertically averaged approaches for CO<sub>2</sub> migration with solubility trapping. *Water Resources Research*, *47*(5), 2010WR009075. <https://doi.org/10.1029/2010WR009075>
- Gasda, S. E., Stephansen, A. F., Aavatsmark, I., & Dahle, H. K. (2013). Upscaled modeling of co<sub>2</sub> injection and migration with coupled thermal processes. *Energy Procedia*, *40*, 384–391. <https://doi.org/10.1016/j.egypro.2013.08.044>
- Gasda, S., Keilegavlen, E., Sandve, T. H., Berge, R., Pettersson, P., & Krumscheid, S. (2022). Practical field-scale simulation approaches for quantification of fault-related leakage under uncertainty. *SSRN Electronic Journal*.  
<https://doi.org/10.2139/ssrn.4277020>
- Gibson, R. G. (1998). Physical character and fluid-flow properties of sandstone-derived fault zones. *Geological Society, London, Special Publications*, *127*(1), 83–97.  
<https://doi.org/10.1144/GSL.SP.1998.127.01.07>
- Gillespie, P. A., Howard, C. B., Walsh, J. J., & Watterson, J. (1993). Measurement and characterisation of spatial distributions of fractures. *Tectonophysics*, *226*(1–4), 113–141. [https://doi.org/10.1016/0040-1951\(93\)90114-Y](https://doi.org/10.1016/0040-1951(93)90114-Y)
- Gilmore, K. A., Sahu, C. K., Benham, G. P., Neufeld, J. A., & Bickle, M. J. (2022). Leakage dynamics of fault zones: Experimental and analytical study with application to CO<sub>2</sub> storage. *Journal of Fluid Mechanics*, *931*, A31.  
<https://doi.org/10.1017/jfm.2021.970>

- Hasbollah, D. Z. A., Junin, R., Taib, A. M., & Mazlan, A. N. (2020). Basin evaluation of co2 geological storage potential in malay basin, malaysia. In P. Duc Long & N. T. Dung (Eds.), *Geotechnics for Sustainable Infrastructure Development* (Vol. 62, pp. 1405–1410). Springer Singapore. [https://doi.org/10.1007/978-981-15-2184-3\\_184](https://doi.org/10.1007/978-981-15-2184-3_184)
- Hepple, R. P., & Benson, S. M. (2005). Geologic storage of carbon dioxide as a climate change mitigation strategy: Performance requirements and the implications of surface seepage. *Environmental Geology*, 47(4), 576–585. <https://doi.org/10.1007/s00254-004-1181-2>
- Herzog, H. J. (2011). Scaling up carbon dioxide capture and storage: From megatons to gigatons. *Energy Economics*, 33(4), 597–604. <https://doi.org/10.1016/j.eneco.2010.11.004>
- Huppert, H. E., & Woods, A. W. (1995). Gravity-driven flows in porous layers. *Journal of Fluid Mechanics*, 292, 55–69. <https://doi.org/10.1017/S0022112095001431>
- Jha, B., & Juanes, R. (2014). Coupled multiphase flow and poromechanics: A computational model of pore pressure effects on fault slip and earthquake triggering. *Water Resources Research*, 50(5), 3776–3808. <https://doi.org/10.1002/2013WR015175>
- Jones, D. G., Beaubien, S. E., Blackford, J. C., Foekema, E. M., Lions, J., De Vittor, C., West, J. M., Widdicombe, S., Hauton, C., & Queirós, A. M. (2015). Developments since 2005 in understanding potential environmental impacts of CO2 leakage from geological storage. *International Journal of Greenhouse Gas Control*, 40, 350–377. <https://doi.org/10.1016/j.ijggc.2015.05.032>
- Kang, M., Nordbotten, J. M., Doster, F., & Celia, M. A. (2014). Analytical solutions for two-phase subsurface flow to a leaky fault considering vertical flow effects and fault properties. *Water Resources Research*, 50(4), 3536–3552. <https://doi.org/10.1002/2013WR014628>
- Kettermann, M., Smeraglia, L., Morley, C. K., Von Hagke, C., & Tanner, D. C. (2020). Fault sealing. In *Understanding Faults* (pp. 283–350). Elsevier. <https://doi.org/10.1016/B978-0-12-815985-9.00008-4>
- Knipe, R. J., Jones, G., & Fisher, Q. J. (1998). Faulting, fault sealing and fluid flow in hydrocarbon reservoirs: An introduction. *Geological Society, London, Special Publications*, 147(1). <https://doi.org/10.1144/GSL.SP.1998.147.01.01>
- Krevor, S., De Coninck, H., Gasda, S. E., Ghaleigh, N. S., De Gooyert, V., Hajibeygi, H., Juanes, R., Neufeld, J., Roberts, J. J., & Swennenhuis, F. (2023). Subsurface carbon dioxide and hydrogen storage for a sustainable energy future. *Nature Reviews Earth & Environment*, 4(2), 102–118. <https://doi.org/10.1038/s43017-022-00376-8>
- Kumar, A., Ozah, R., Noh, M., Pope, G. A., Bryant, S., Sepehrnoori, K., & Lake, L. W. (2005). Reservoir simulation of co2 storage in deep saline aquifers. *SPE Journal*, 10(03), 336–348. <https://doi.org/10.2118/89343-PA>
- Lie, K.-A. (2019). *An introduction to reservoir simulation using matlab/gnu octave: User guide for the matlab reservoir simulation toolbox(Mrst)* (1st ed.). Cambridge University Press. <https://doi.org/10.1017/9781108591416>
- Malaysian Continental Shelf Project, National Security Council, Malaysia, Madon, M., Jong, J., & JX Nippon Oil and Gas Exploration (Malaysia) Limited, Malaysia. (2021). Geothermal gradient and heat flow maps of offshore malaysia: Some updates and observations. *Bulletin of the Geological Society of Malaysia*, 71, 159–183. <https://doi.org/10.7186/bgsm71202114>
- Manzocchi, T., Childs, C., & Walsh, J. J. (2010). Faults and fault properties in hydrocarbon flow models. *Geofluids*, 10(1–2), 94–113. <https://doi.org/10.1111/j.1468-8123.2010.00283.x>

- Manzocchi, T., Walsh, J. J., Nell, P., & Yielding, G. (1999). Fault transmissibility multipliers for flow simulation models. *Petroleum Geoscience*, 5(1), 53–63. <https://doi.org/10.1144/petgeo.5.1.53>
- Meguerdijian, S., & Jha, B. (2021). Quantification of fault leakage dynamics based on leakage magnitude and dip angle. *International Journal for Numerical and Analytical Methods in Geomechanics*, 45(16), 2303–2320. <https://doi.org/10.1002/nag.3267>
- Michie, E. A. H., Mulrooney, M. J., & Braathen, A. (2021). Fault interpretation uncertainties using seismic data, and the effects on fault seal analysis: A case study from the Horda Platform, with implications for CO<sub>2</sub> storage. *Solid Earth*, 12(6), 1259–1286. <https://doi.org/10.5194/se-12-1259-2021>
- Mitchell, T. M., & Faulkner, D. R. (2012). Towards quantifying the matrix permeability of fault damage zones in low porosity rocks. *Earth and Planetary Science Letters*, 339–340, 24–31. <https://doi.org/10.1016/j.epsl.2012.05.014>
- Møll Nilsen, H., Herrera, P. A., Ashraf, M., Ligaarden, I., Iding, M., Hermanrud, C., Lie, K.-A., Nordbotten, J. M., Dahle, H. K., & Keilegavlen, E. (2011). Field-case simulation of CO<sub>2</sub> plume migration using vertical-equilibrium models. *Energy Procedia*, 4, 3801–3808. <https://doi.org/10.1016/j.egypro.2011.02.315>
- Møll Nilsen, H., Lie, K.-A., & Andersen, O. (2015). Analysis of CO<sub>2</sub> trapping capacities and long-term migration for geological formations in the Norwegian North Sea using MRST-co2lab. *Computers & Geosciences*, 79, 15–26. <https://doi.org/10.1016/j.cageo.2015.03.001>
- Møyner, O., & Nilsen, H. M. (2019). Multiresolution coupled vertical equilibrium model for fast flexible simulation of CO<sub>2</sub> storage. *Computational Geosciences*, 23(1), 1–20. <https://doi.org/10.1007/s10596-018-9775-z>
- Neufeld, J. A., Vella, D., & Huppert, H. E. (2009). The effect of a fissure on storage in a porous medium. *Journal of Fluid Mechanics*, 639, 239–259. <https://doi.org/10.1017/S0022112009991030>
- Nilsen, H. M., Lie, K.-A., & Andersen, O. (2016). Fully-implicit simulation of vertical-equilibrium models with hysteresis and capillary fringe. *Computational Geosciences*, 20(1), 49–67. <https://doi.org/10.1007/s10596-015-9547-y>
- Nilsen, H. M., Lie, K.-A., & Andersen, O. (2016). Robust simulation of sharp-interface models for fast estimation of CO<sub>2</sub> trapping capacity in large-scale aquifer systems. *Computational Geosciences*, 20(1), 93–113. <https://doi.org/10.1007/s10596-015-9549-9>
- Nordbotten, J. M., & Celia, M. A. (2011). *Geological storage of CO<sub>2</sub>: Modeling approaches for large-scale simulation* (1st ed.). Wiley. <https://doi.org/10.1002/9781118137086>
- Nordbotten, J. M., & Dahle, H. K. (2011). Impact of the capillary fringe in vertically integrated models for CO<sub>2</sub> storage. *Water Resources Research*, 47(2), 2009WR008958. <https://doi.org/10.1029/2009WR008958>
- Oladyshkin, S., Class, H., Helmig, R., & Nowak, W. (2011). A concept for data-driven uncertainty quantification and its application to carbon dioxide storage in geological formations. *Advances in Water Resources*, 34(11), 1508–1518. <https://doi.org/10.1016/j.advwatres.2011.08.005>
- Pawar, R. J., Bromhal, G. S., Carey, J. W., Foxall, W., Korre, A., Ringrose, P. S., Tucker, O., Watson, M. N., & White, J. A. (2015). Recent advances in risk assessment and risk management of geologic CO<sub>2</sub> storage. *International Journal of Greenhouse Gas Control*, 40, 292–311. <https://doi.org/10.1016/j.ijggc.2015.06.014>
- Pawar, R. J., Bromhal, G. S., Chu, S., Dilmore, R. M., Oldenburg, C. M., Stauffer, P. H., Zhang, Y., & Guthrie, G. D. (2016). The National Risk Assessment Partnership's integrated assessment model for carbon storage: A tool to support decision making

- amidst uncertainty. *International Journal of Greenhouse Gas Control*, 52, 175–189. <https://doi.org/10.1016/j.ijggc.2016.06.015>
- Pei, Y., Paton, D. A., Knipe, R. J., & Wu, K. (2015). A review of fault sealing behaviour and its evaluation in siliciclastic rocks. *Earth-Science Reviews*, 150, 121–138. <https://doi.org/10.1016/j.earscirev.2015.07.011>
- Petrie, E. S., Petrie, R. A., & Evans, J. P. (2014). Identification of reactivation and increased permeability associated with a fault damage zone using a multidisciplinary approach. *Journal of Structural Geology*, 59, 37–49. <https://doi.org/10.1016/j.jsg.2013.11.008>
- Pettersson, P., Keilegavlen, E., Sandve, T. H., Gasda, S. E., & Krumscheid, S. (2025). Copula modeling and uncertainty propagation in field-scale simulation of CO<sub>2</sub> fault leakage. *Water Resources Research*, 61(1), e2024WR038073. <https://doi.org/10.1029/2024WR038073>
- Phillips, T., Kampman, N., Bisdom, K., Forbes Inskip, N. D., Den Hartog, S. A. M., Cnudde, V., & Busch, A. (2020). Controls on the intrinsic flow properties of mudrock fractures: A review of their importance in subsurface storage. *Earth-Science Reviews*, 211, 103390. <https://doi.org/10.1016/j.earscirev.2020.103390>
- Pruess, K. (2011). Integrated modeling of CO<sub>2</sub> storage and leakage scenarios including transitions between super- and subcritical conditions, and phase change between liquid and gaseous CO<sub>2</sub>. *Greenhouse Gases: Science and Technology*, 1(3), 237–247. <https://doi.org/10.1002/ghg.24>
- Ramachandran, H., Pope, G. A., & Srinivasan, S. (2017). Numerical study on the effect of thermodynamic phase changes on CO<sub>2</sub> leakage. *Energy Procedia*, 114, 3528–3536. <https://doi.org/10.1016/j.egypro.2017.03.1482>
- Ramachandran, H. (2025). Poriylar/faultve: faultve (v1.0). Software for article “Rapid Fault Leakage Modelling for CO<sub>2</sub> Storage in Saline Aquifers” [Software]. *Zenodo*. <https://doi.org/10.5281/zenodo.17469206>
- Rinaldi, A. P., Rutqvist, J., & Cappa, F. (2014). Geomechanical effects on CO<sub>2</sub> leakage through fault zones during large-scale underground injection. *International Journal of Greenhouse Gas Control*, 20, 117–131. <https://doi.org/10.1016/j.ijggc.2013.11.001>
- Ringrose, P. S., & Meckel, T. A. (2019). Maturing global CO<sub>2</sub> storage resources on offshore continental margins to achieve 2DS emissions reductions. *Scientific Reports*, 9(1), 17944. <https://doi.org/10.1038/s41598-019-54363-z>
- Ringrose, P., & Bentley, M. (2021). *Reservoir model design: A practitioner's guide*. Springer International Publishing. <https://doi.org/10.1007/978-3-030-70163-5>
- Rizzo, R. E., Inskip, N. F., Fazeli, H., Betlem, P., Bisdom, K., Kampman, N., Snippe, J., Senger, K., Doster, F., & Busch, A. (2024). Modelling geological CO<sub>2</sub> leakage: Integrating fracture permeability and fault zone outcrop analysis. *International Journal of Greenhouse Gas Control*, 133, 104105. <https://doi.org/10.1016/j.ijggc.2024.104105>
- Romanak, K., & Dixon, T. (2022). CO<sub>2</sub> storage guidelines and the science of monitoring: Achieving project success under the California Low Carbon Fuel Standard CCS Protocol and other global regulations. *International Journal of Greenhouse Gas Control*, 113, 103523. <https://doi.org/10.1016/j.ijggc.2021.103523>
- Rutqvist, J. (2012). The geomechanics of CO<sub>2</sub> storage in deep sedimentary formations. *Geotechnical and Geological Engineering*, 30(3), 525–551. <https://doi.org/10.1007/s10706-011-9491-0>
- Saló-Salgado, L., Davis, S., & Juanes, R. (2023). Fault permeability from stochastic modeling of clay smears. *Geology*, 51(1), 91–95. <https://doi.org/10.1130/G50739.1>

- Sayag, R., & Neufeld, J. A. (2016). Propagation of viscous currents on a porous substrate with finite capillary entry pressure. *Journal of Fluid Mechanics*, 801, 65–90. <https://doi.org/10.1017/jfm.2016.412>
- Seebeck, H., Nicol, A., Walsh, J. J., Childs, C., Beetham, R. D., & Pettinga, J. (2014). Fluid flow in fault zones from an active rift. *Journal of Structural Geology*, 62, 52–64. <https://doi.org/10.1016/j.jsg.2014.01.008>
- Sibson, R. H. (1977). Fault rocks and fault mechanisms. *Journal of the Geological Society*, 133(3), 191–213. <https://doi.org/10.1144/gsjgs.133.3.0191>
- Silva, J. A., Saló-Salgado, L., Patterson, J., Dasari, G. R., & Juanes, R. (2023). Assessing the viability of CO<sub>2</sub> storage in offshore formations of the Gulf of Mexico at a scale relevant for climate-change mitigation. *International Journal of Greenhouse Gas Control*, 126, 103884. <https://doi.org/10.1016/j.ijggc.2023.103884>
- Simpson, G., Guéguen, Y., & Schneider, F. (2001). Permeability enhancement due to microcrack dilatancy in the damage regime. *Journal of Geophysical Research: Solid Earth*, 106(B3), 3999–4016. <https://doi.org/10.1029/2000JB900194>
- Snippe, J., Kampman, N., Bisdorf, K., Tambach, T., March, R., Maier, C., Phillips, T., Inskip, N. F., Doster, F., & Busch, A. (2022). Modelling of long-term along-fault flow of CO<sub>2</sub> from a natural reservoir. *International Journal of Greenhouse Gas Control*, 118, 103666. <https://doi.org/10.1016/j.ijggc.2022.103666>
- Tewari, R. D., Tan, C. P., & Sedaralit, M. F. (2023). A toolkit approach for carbon capture and storage in offshore depleted gas field. *American Journal of Environmental Sciences*, 19(1), 8–42. <https://doi.org/10.3844/ajessp.2023.8.42>
- Tueckmantel, C., Fisher, Q. J., Manzocchi, T., Skachkov, S., & Grattoni, C. A. (2012). Two-phase fluid flow properties of cataclastic fault rocks: Implications for CO<sub>2</sub> storage in saline aquifers. *Geology*, 40(1), 39–42. <https://doi.org/10.1130/G32508.1>
- Vilarrasa, V., Makhnenko, R. Y., & Laloui, L. (2017). Potential for fault reactivation due to CO<sub>2</sub> injection in a semi-closed saline aquifer. *Energy Procedia*, 114, 3282–3290. <https://doi.org/10.1016/j.egypro.2017.03.1460>
- Walsh, J. J., Watterson, J., Heath, A. E., & Childs, C. (1998). Representation and scaling of faults in fluid flow models. *Petroleum Geoscience*, 4(3), 241–251. <https://doi.org/10.1144/petgeo.4.3.241>
- Yielding, G., Bretan, P., & Freeman, B. (2010). Fault seal calibration: A brief review. *Geological Society, London, Special Publications*, 347(1), 243–255. <https://doi.org/10.1144/SP347.14>
- Yortsos, Y. C. (1995). A theoretical analysis of vertical flow equilibrium. *Transport in Porous Media*, 18(2), 107–129. <https://doi.org/10.1007/BF01064674>
- Zhao, X., & Jha, B. (2019). Role of well operations and multiphase geomechanics in controlling fault stability during CO<sub>2</sub> storage and enhanced oil recovery. *Journal of Geophysical Research: Solid Earth*, 124(7), 6359–6375. <https://doi.org/10.1029/2019JB017298>
- Zheng, X., & Espinoza, D. N. (2022). Stochastic quantification of CO<sub>2</sub> fault sealing capacity in sand-shale sequences. *Marine and Petroleum Geology*, 146, 105961. <https://doi.org/10.1016/j.marpetgeo.2022.105961>